In vitro Microtubule Tip Tracking: A quantitative study of the accuracy and precision.

by

Nils Gustafsson

CoMPLEX - University College London

Supervised by: Dr Thomas Surrey and Dr Lewis Griffin

Thesis submitted for the degree of

Master of Research

University College London

August 2014

Declaration

I Nils Gustafsson confirm that the work presented in this thesis is my own. Where information has been derived from other sources, I confirm that this has been indicated in the thesis.

X

Nils Gustafsson
Mr

Abstract:

A new method for the simulation of TIRF microscopy data of dynamic microtubules is presented and validated. This method makes use of direct rendering of Gaussians onto a pixel grid rather than the convolution of a high resolution image followed by down sampling. This new simulation method is used to analyse the accuracy and precision of a microtubule end tracking algorithm. It is shown that the main parameter in determining the precision in tracking is the signal to noise ratio which is normally distributed and has zero mean so the accuracy is still very good. I also derive a correction to the mean squared displacement to take account of the finite exposure time of the camera given the case of directed diffusion.

Contents

List of Figures

Abbreviations

MT	Microtubule
MAP	Microtubule associated Protein
+TIP	Plus end tracking protein

EB	End binding protein (for example EB1, EB2, and EB3 in humans)
EMCCD	Electron-multiplying charge-coupled device
fps	Frames per second
GFP	Green fluorescent protein
TIRF	Total internal reflection microscopy
MAL3	*S. pombe* homologue of the human EB1 protein.
GTP	Tri-phosphate
GDP	Di-phosphate
SNR	Signal to noise ratio
MDA	Microtubule Dynamics Analysis

1 Introduction

Microtubules (MTs) are one of the three main filament like protein polymers which form the cytoskeleton of all eukaryotic cells (**Figure 1**C). This introduction is not a substitute for the thorough description which can be found in any standard cell biology text book such as *The Molecular biology of the cell*[1,2] and in the recent review by Wade et. al., 2009[3] and the references therein.

MTs are hollow proteinous tubes with an outer diameter of ≈25nm composed of a non-covalently bonded lattice of α-tubulin β-tubulin heterodimer subunits (**Figure 1**A,D). They are relatively long and stiff and typically originate from a small organising structure at the centre of the cell called the centrosome and extend out towards the cell periphery. MTs are intrinsically polar with a plus end where β-tubulin is exposed in contrast to the minus end where α-tubulin is exposed[4].

As part of the cytoskeleton MTs contribute to the formation of scaffold structures which impart mechanical stability to the cell. Specifically, MTs have an organising role and are responsible for anchoring organelles and provide the framework for guiding directed intracellular transport via MT associated motor proteins.

The static view of MTs barely scratches the surface of their functional importance to cell biology as MTs are highly dynamic. They can quickly disassemble and reassemble elsewhere and the natural state of MTs is to stochastically switch between phases of growth and shrinkage (dynamic instability) (**Figure 1**B,E)[5,6]. Typically the plus end is more dynamic with the minus end anchored in the centrosome from where MTs are nucleated. These dynamics are finely controlled by many microtubule associated proteins (MAPs). Some MAPs for example bind and stabilise the growing end creating a semi-permanent bridge between the centrally located centrosome and the location of the MAP. This constant random exploration and selective capture of MTs creates a highly organised network of MTs linking selected parts of the cellular environment[7]. Furthermore the regulation of microtubule dynamics in axons and dendrites is a key determinant of neuronal polarity and differentiation and probably contributes significantly to neuronal plasticity[8].

The dynamic nature of MTs and the intricate control conveyed by MAPs is acutely demonstrated when cells enter mitosis (**Figure 1**C). The entire MT network rapidly disassembles and reforms into an intricate structure known as the mitotic spindle responsible for segregating chromosomes equally. Drugs such as vinca alkaloids and taxanes which prevent MT polymerisation and depolymerisation respectively have a profound effect on the formation of the mitotic spindle. In some cases this allows preferential killing of rapidly dividing cells such as are present in many cancers. There are many examples of tubulin targeted therapeutic drugs used in the treatment of gout and arterial restenosis

and particularly in chemotherapy[3,9,10]. In addition to being targets for cancer treatment, the regulation of MT dynamics in chromosome separation and cytokinesis is clearly important in the development of cancers. Ranked by the correlation of gene expression to a measure of chromosome instability, the 3 of the 4 highest ranked genes code for MAPs and the 4th codes of a transcriptional regulator of MAPs. An array of other genes associated with chromosome separation appear in the top 70 of the 10,151 genes studied[11]. Chromosome instability is a strong predictor of clinical outcome in multiple human cancers and this correlation is replicated across multiple tumour types indicating misregulation of MT dynamics is a probable cause of cancer.

The mechanisms governing MT assembly kinetics, dynamic instability and MAP interactions are only poorly understood despite being the subject of intensive research for some three decades. High resolution methods such as X-ray crystallography and electron microscopy provide insights into the structure of the key components[12–14] but are labour intensive and provide a less satisfactory description of dynamics. Eukaryotic cell culture and live cell fluorescence microscopy allows the visualisation of dynamics *in vivo* but limited to resolutions >200nm,[15] much larger than the diameter of a MT filament (≈25nm). Furthermore, the number of components associated with MT dynamics is too large to be understood currently on a system wide level *in vivo*. To overcome these issues reductionist bottom up approaches of *in vitro* reconstruction from purified proteins studied by total internal reflection florescence (TIRF) microscopy have become popular techniques[16]. Recent advances in fluorescence microscopy and associated computational methods have greatly enhanced conventional microscopy allowing quantitative biological measurements on the nanometre scale via the accurate localisation of individual fluorescent probes[17,18]. These methods have been expanded to allow the automated tracking and localisation of MT filaments and their end positions with nanometre scale precision revealing much about MT dynamics[19–21]. Furthermore the accurate referencing, alignment and subsequent averaging of an entire population of MTs, imaged by multi-channel fluorescence microscopy, allows the spatial distribution of the interaction of a MAP to be studied, relative to the growing MT end [22].

In the case of single particle localisation and tracking, the accuracy (closeness to the true location) and precision (the reproducibility of measured locations) of the approach have been extensively studied[23–25]. Note that the term accuracy will be used to describe both accuracy and precision unless otherwise stated. The accuracy and precision of automated filament localisation and end position tracking methods however, are much less well characterised. As such the question of how accurately the MT end (otherwise called MT tip) can be localised remains unsatisfactorily answered.

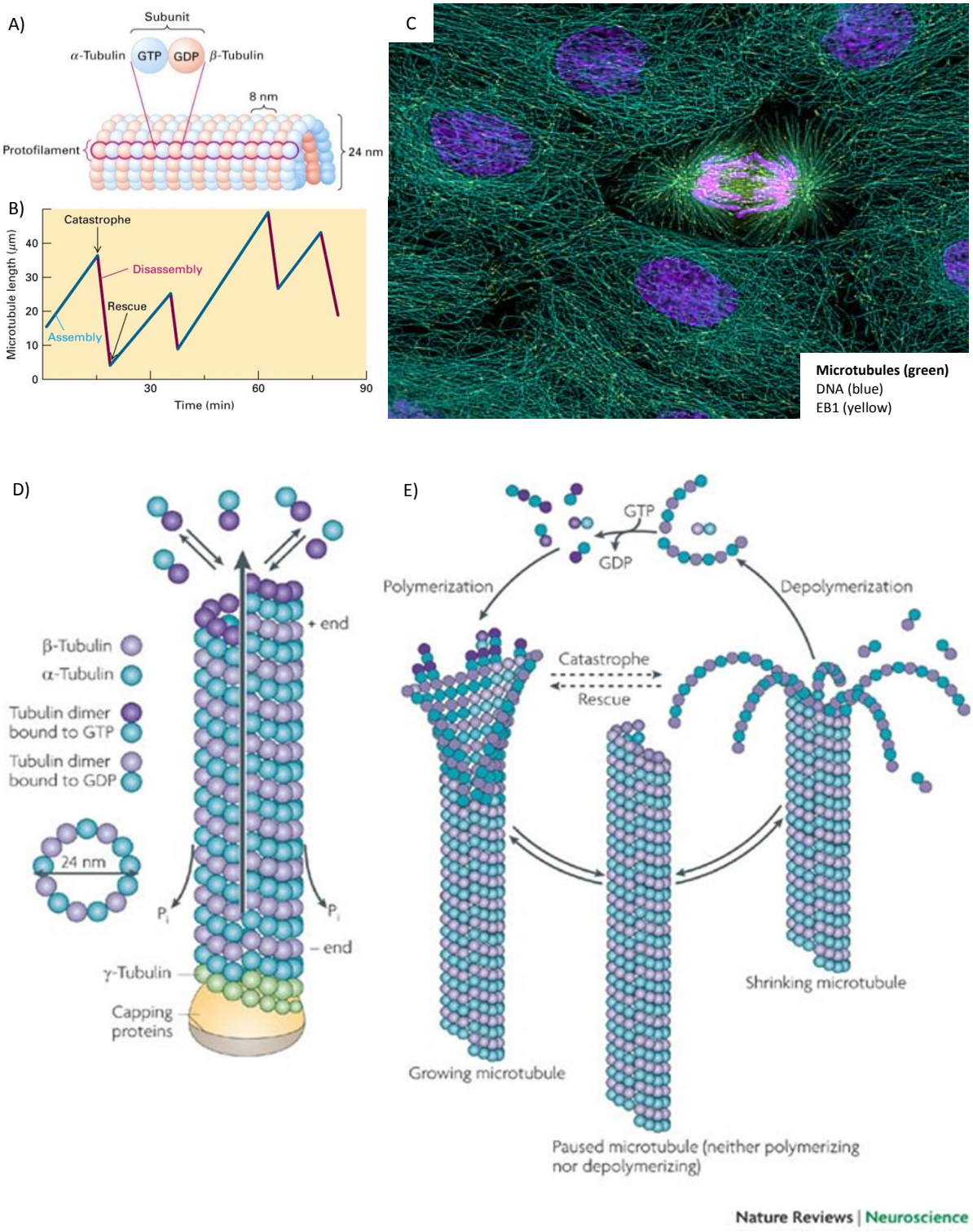

Figure 1: Microtubules. A) and D) show schematic representations of the microtubule lattice. B) shows a schematic representations of a microtubule length against time trace demonstrating the property of dynamic instability. E) shows a schematic representation of the various states a microtubule can switch between stochastically giving rise to dynamic instability. C) is a fluorescence microscopy image of interphase cells surrounding a mitotic cell with microtubules (green), DNA (blue) and EB1 (yellow). The mitotic spindle can clearly be seen with astral microtubules radiating away from two centre points of daughter cells and the mid-zone spindle part way through chromosome separation. A) and B) were taken from *Molecular Cell Biology* [2]. C) was taken from wittmann.ucsf.edu, UCSF, 2013. D) and E) were taken from [8].

Accurate tracking of MT end positions over time facilitates the testing of statistical descriptions of these dynamics. Mean square displacement (MSD) analysis, a standard analysis method for single diffusing particles[25] has been used previously[19] for determining an effective diffusion parameter for the dynamic MT tip. In the case of single particle tracking however this method has been shown to be very sensitive to a number of experimental conditions and data fitting methods[23] none of which have been satisfactorily considered for the purposes of the specific MT geometry and experimental conditions.

Simulation of experimental TIRF microscopy data of dynamic MTs provides a "ground truth" data set against which the accuracy of a new tip tracking algorithm can be determined[20]. In order to simulate data and analyse the algorithm's accuracy a good understanding of MT structure and dynamics, the experimental methods and the tip tracking algorithm itself are required. The following section (1.1) outlines the structural and dynamic aspects of MTs which are of particular importance. Section 1.2 describes methods for collecting time-lapse movies of dynamic MTs and the tracking algorithm.

The results of MT end tracking can be used to inform models of MT polymerisation kinetics and via analysis such as MSD. Section 1.3 outlines current approaches to modelling microtubule dynamics and introduces MSD analysis.

The key result presented, is the development of a method for simulating TIRF microscopy image sequences of *in vitro* MTs. Where this method differs from previous simulations of microscope data is in the ability to include MT dynamics within the exposure time of the camera. It is also computationally more efficient and, on the nm scale, truer to the imaging process. This is an aspect that will become significantly more important as current generations of microscopes are able to achieve nm resolution[26]. This simulation data is subsequently used to evaluate the precision and accuracy of Microtubule Dynamics Analysis (MDA) a new microtubule tip tracking algorithm[27]. The Accuracy of tip localisation under experimental conditions is shown to be as little as 1nm laterally and less than 5nm axially, with precisions of 13nm and 40nm respectively. The tracks of the simulated data were analysed by MSD leading to an empirically determined fitting procedure, specific for MT ends. Finally, the derivation of the exposure time effect on the mean squared displacement, published by Michalet, (2010)[23] for Brownian motion in an isotropic medium[28], is extended to describe the directed diffusion of the MT end.

1.1 Microtubules

1.1.1 Microtubule Structure

MTs are long, relatively stiff, hollow cylinders that consist of, typically, 13 protofilaments (**Figure 1**A). Each protofilament is a longitudinal, non-covalently bonded polymer of tubulin heterodimers. Each

tubulin heterodimer accounts for a length of ≈8nm and is formed from two similar globular proteins, α-tubulin and β-tubulin. The protofilaments have a structural polarity with the α-tubulin at the minus end and β-tubulin at the plus end. This polarity is the same for all the protofilaments in the MT giving rise to the polarity of the MT itself. γ-tubulin ring complexes in centrosomes serve as nucleation sites for MT growth. Lateral contacts between protofilaments, thought to be weaker than axial contacts[29], promote the formation of a cylinder which predominantly has a configuration called a B lattice (**Figure 1**D)[10]. The majority of lateral contacts (12 of 13 per tubulin monomer layer) consist of α-α tubulin or β-β tubulin interactions. The final lateral contact is an α-β tubulin interaction and forms a seam in the direction of the MT (**Figure 1**D). It follows that this configuration necessitates a helical structure to the lattice. The most common arrangement is a 3 start helix where a single monomer layer in the MT lattice meets either side of the seam three monomers (1.5 heterodimer subunits) apart[10].

The mechanical properties of the MT filament have been extensively studied with respect to confirming their suitability to the roles they perform within the cell[30–32]. These properties must be accounted for when analysing *in vitro* studies of MT dynamics as thermal fluctuations in the forces acting on the MT deform the filament resulting in significant displacements of the tip position. Briefly, MT mechanical properties can be approximated by a thin flexible rod described by a "beam equation"[33] which states that the bending moment is equal to the bending stiffness (flexural rigidity) times the curvature. Thermally driven fluctuations in MT shape analysed in this way yield estimates of flexural rigidity of the order of $10^{-23} Nm^2$, corresponding to a persistence length of ≈5000μm or a homogeneous, isotropic material of Young's modulus ≈1.2 GPa. Additionally, MTs are expected to be practically inextensible.

A number of co-crystal structures suggest that the α,β tubulin heterodimer subunit has a curvature of approximately 12 degrees in solution and that this curvature is independent of the associated nucleotide[34]. The lateral bonds of the MT lattice appear to be responsible for the unbending of the subunit, enabling the formation of a straight filament. At the less stable, growing or shrinking ends this is a possible cause of the high degree of variability in the MT tip structure that has been observed (**Figure 2**a)[35].

MT ends can exhibit differing lengths of protofilaments, called "tapering", especially prominent in mammalian cells (**Figure 2**b,c), resulting in sheet like or individual protruding protofilaments. The simplest end structure observed is the blunt case where the number of lateral contacts is maximised but there are many configurations containing a large number of subunits with one or even zero lateral contacts. These structures are too small to be resolved directly using current fluorescent microscopy methods. Indirectly they can be inferred from the broadening of the axial end profile of the

fluorescence signal caused by the decreasing density of tubulin subunits in the tapered end. This has been shown previously in simulations[20,22] and in cells[20].

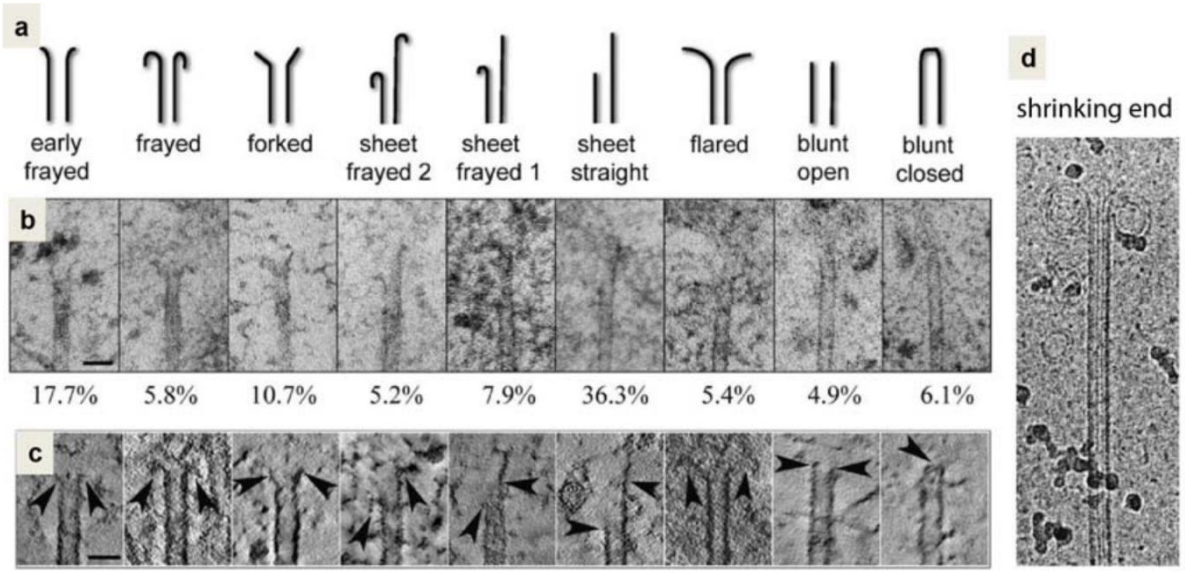

Figure 2: Microtubule end structures. *a) is a schematic representation of observed MT tip structures. b) Electron micrographs and c) tomographical slices 5nm thick show the different MT tip structures observed in mouse fibroblasts. The scale bar is 50nm. The relative abundances of structures of each type is indicated in percent. d) is and election micrograph of a depolymerising MT. Taken from* [45].

1.1.2 Microtubule Dynamics

It is known that under normal circumstances no tubulin is added or lost from the MT lattice at any point other than the terminal ends[1]. There is however, a coexistence of assembly and disassembly at the plus end of a MT with α,β tubulin subunits stochastically added and lost at the extreme end of each protofilament[36]. During polymerisation both α-tubulin and β-tubulin are typically GTP bound although GDP tubulin addition in small amount has been reported[37]. It is not known why GTP bound tubulin is polymerisation competent but GDP bound tubulin is not although the nucleotide possibly has an effect on the strength of the lateral bonds[14,38]. The GTP bound to α-tubulin is relatively stable however the GTP bound to β-tubulin is hydrolysed shortly after incorporation to the MT lattice. Unlike GTP bound tubulin GDP bound tubulin is prone to depolymerisation, when the GDP bound tubulin is exposed at the MT end it appears to adopt a curved structure, similar to when in solution, promoting depolymerisation. If net addition of subunits is faster than the hydrolysis of GTP bound to β-tubulin a protective cap of GTP bound tubulin prevents the rapid depolymerisation of the MT. When GTP hydrolysis reaches the end of the MT, either stochastically or following a pause in growth, rapid depolymerisation occurs[39,40]. This switch from growth to shrinkage is called catastrophe and can result in the depolymerisation of the entire MT. The formation of a new GTP cap can occur however, halting depolymerisation, this is called rescue.

The microtubule tip structure is very likely to play a major role in the polymerisation and depolymerisation kinetics as well as determining catastrophe frequencies. This is because in the blunt case (**Figure 2**) all subunits at the end of the MT have one axial contact and two lateral contacts and the probability that a subunit is added or lost from any of the protofilaments is equal. With more tapered ends however, steric hindrances to the diffusion of free tubulin by longer protofilaments and protofilament sheets reduce the probability that a subunit will be added to one of the shorter protofilaments[29]. In turn the longest protofilaments, while maintaining a single axial contact may only have one or in some cases no lateral contacts increasing the probability of losing subunits from longer protofilaments[19]. The result is that taper lengths appear to increase as the MT grows in length, known as "MT aging"[41]. This is accompanied by an increased catastrophe frequency[42] and instability caused by increased taper length has been proposed as the reason for increased catastrophe frequencies over time, however there is currently little consensus on MT dynamic instability[43–46]. Furthermore, some evidence also suggests that MAPs can modify the end structure thereby controlling MT dynamics[47]. These are typically a subset of MAPs called +TIPs which only bind to the growing end of MTs[48] and are one method for roughly tracking the end position of MTs.

1.2 Microtubule Tip Tracking

The underlying molecular mechanisms which give rise to the dynamic properties of MTs and their regulation are inherently stochastic. The study of stochastic processes requires a large number of reproducible quantitative measurements in order build a statistical description of the process. For this reason it is important to be able to make quantitative measures of MT properties across multiple growth episodes of an entire population of many microtubules, requiring automation. The natural choice of measurement to make is of the MT end position over time, from which polymerisation and depolymerisation kinetics such as growth velocities and fluctuations can be inferred through techniques such as mean displacement and mean square displacement analysis. The end position also provides a reference point on the MT to which multiple frames from multiple time-lapse image sequences can be aligned. These aligned frames can then be averaged providing nanometre precision average end structures and MAP binding site distributions.

1.2.1 Experimental Methods

Tubulin is purified from pigs brain and a small fraction is labelled with a fluorescence dye, typically Cy5, as described[49,50]. Only a small fraction of the tubulin is labelled because using a high ratio of labelled tubulin has been shown to negatively impact on the MT's polymerisation kinetics. *In vitro* assays were performed as described by Bieling et. al. (2010)[16]. Briefly, a short MT is grown using GMPCPP, a non-hydrolysable analogue of GTP, the use of which prevents depolymerisation. This short

stabilised MT is biotinilated and bound to a biotinilated coverslip via neutravidin linkers (**Figure 3**a). Free tubulin, GTP, suitable buffer conditions and GFP labelled MAPs can be introduced in a controlled manor via microfluidics. The temperature was 30°C. Simultaneous dual-colour time-lapse imaging of the Cy5 MT channel and GFP MAP channel was performed on an iMIC (TILL Photonics, Germany) total internal reflection fluorescence (TIRF) microscope equipped with a 100x 1.49 N.A (Olympus, Japan) objective lens. Cy5 and GFP light paths were separated using a quadband dichroic mirror (405/488/561/64, Semrock, USA), and GFP (525/50, Semrock, USA) and Cy5 (700/75, Semrock, USA) emission filters. Images were recorded with a 300ms exposure times at a frame rate of 2 frames per second (fps) onto Evolve 512 (Photometrics, UK) EMCCD cameras. The sample was illuminated with 488nm and 640nm diode lasers (Toptica, Germany). The two channels were aligned using registration of images of a standard calibration grid with 500nm features (Compugraphics, UK) recorded simultaneously using bright-field illumination. Image controls were performed using 100 nm TetraSpeck (Invitrogen, UK) fluorescent beads simultaneously in both the Cy5 and GFP channels.

1.2.2 Previous Tip Tracking Methods and Algorithms

A number of automatic tracking routines have recently been developed with the most common method being the use of +TIP MAPs as reporter molecules for the MT end. The MAP-GFP channel typically has a much higher signal to noise ratio (SNR) due to the much lower concentrations of free MAP-GFP in the imaging environment. This imparts a much better contrast to the image than can be achieved in the MT-Cy5 channel images facilitating the direct use of robust single particle tracking algorithms[51,52]. This method is in use in both live cell imaging and *in vitro* imaging and frequently makes use of the end binding (EB) family of proteins or their *S. pombe* homologue Mal3 (**Figure 3**).

The use of a reporter molecule such as EB1 or Mal3 can be very effective however the ideal case would be to track the microtubule ends themselves. One reason for this is that EBs accumulate at polymerising, but not pausing or depolymerising MT ends so the end position cannot be determined for the entire microtubule life history. Another reason is that EBs have been reported as having nanometre scale variations in binding site distributions relative to the MT end[22]. It is only possible to determine this when the MT end position and the EB position are determined independently.

One of the first solutions for direct tracking of microtubule ends relied on determining the microtubule orientation and extracting the one-dimensional intensity profile along the microtubule axis. This intensity profile is fitted using a one dimensional model derived from the convolution of the PSF with a prediction of the MT end structure[20,53]. This method was reported to fit the end position axially with a precision of ≈36nm. Alternatively, a two-dimensional model can be used to directly fit the image data, overcoming limitations introduced in transformations required (such as interpolation) in 1D

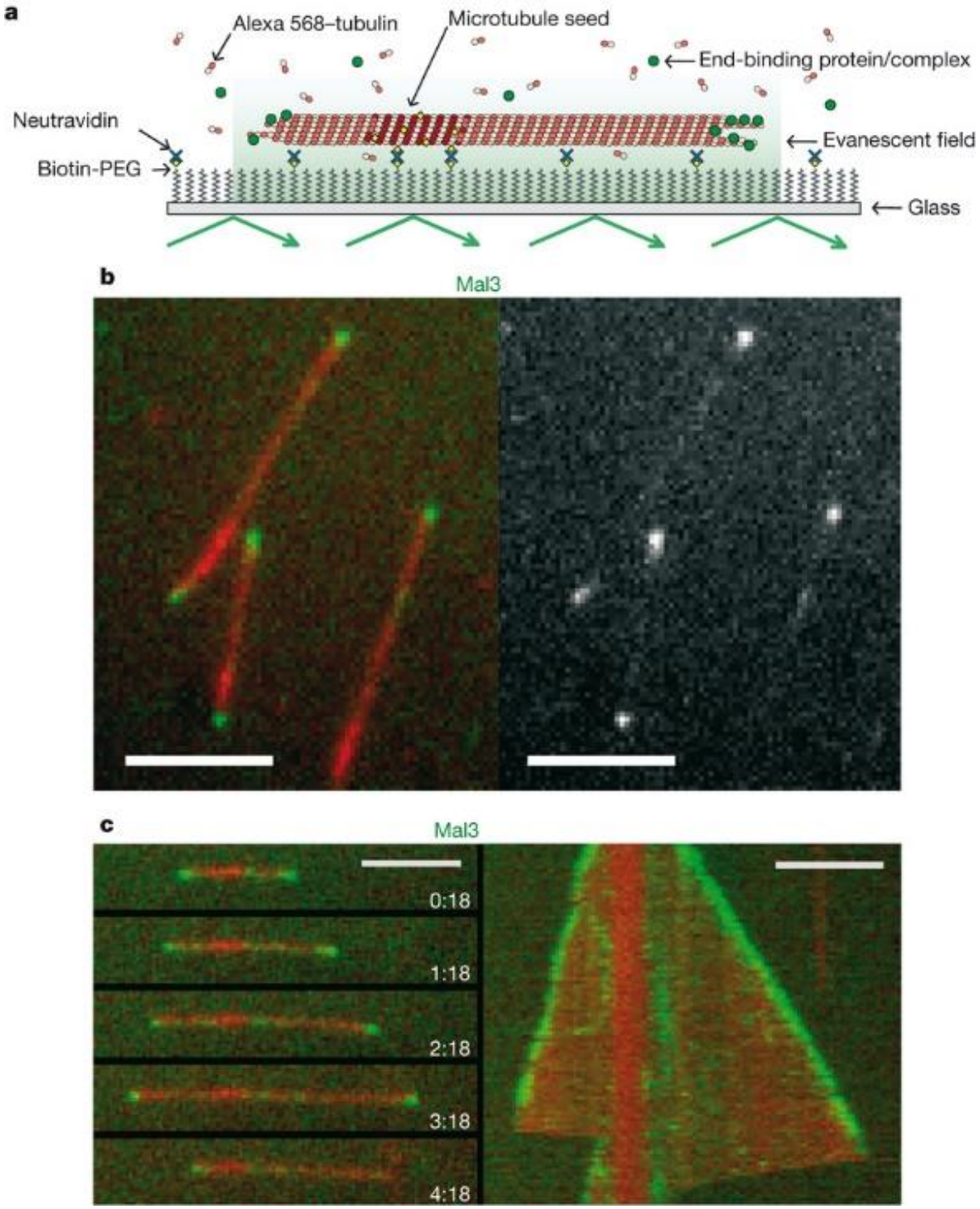

Figure 3: Tracking of growing microtubule ends with MAL3 in vitro. *a) is a schematic representation of the experimental setup used. A biotinilated, non-hydrolysable, stable seed is attached to the cover slip and fluorescently labelled tubulin is introduced in solution, together with MAPs and appropriate buffers. b) (left) Superimposed fluorescence microscope images of +TIP binding MAP Mal3 (green) and dynamic MTs (red). (right) Mal3 channel only demonstrating superior contrast and signal to noise ratio. c) (left) A time sequence of a dynamic MT. (right) a kymograph showing a 5 min period of growth including a catastrophe. In Vitro, the minus end is not capped so also grows (left of the brightly labelled seed), however the rate is slower. Scale Bars indicate 5µm. Figure taken from Bieling et. al., (2007)*[52]

methods[21]. 2D fitting has yielded a precision of the order of ≈10nm in experiment however, these experiments were done using stabilised MTs with no free tubulin in the image volume and consequently the images used had a very high SNR. In order to use this 2D fitting method with dynamic MTs at the low SNR typical when free tubulin is added to the imaging volume, a number of pre-processing steps have been added along with a number of post processing analysis functions to form the MATLAB program Microtubule Dynamics Analysis (MDA)[22,27].

1.2.3 Microtubule Dynamics Analysis Tip Tracking Algorithm

After marking of the microtubule in the first frame of an image sequence, MDA follows an automated process (**Figure 4**)[27]. A Wallis filter is applied to every image to equalise the local contrast across images to facilitate the rough determination of position and extent of the microtubule. This rough position is determined by two steps. The backbone is identified first by allowing lateral variation in tracked positions from the previous frame and identifying the brightest pixels in the smoothed image. This enables tracking of drifting MTs and MTs significantly deflected between frames by thermal fluctuations.

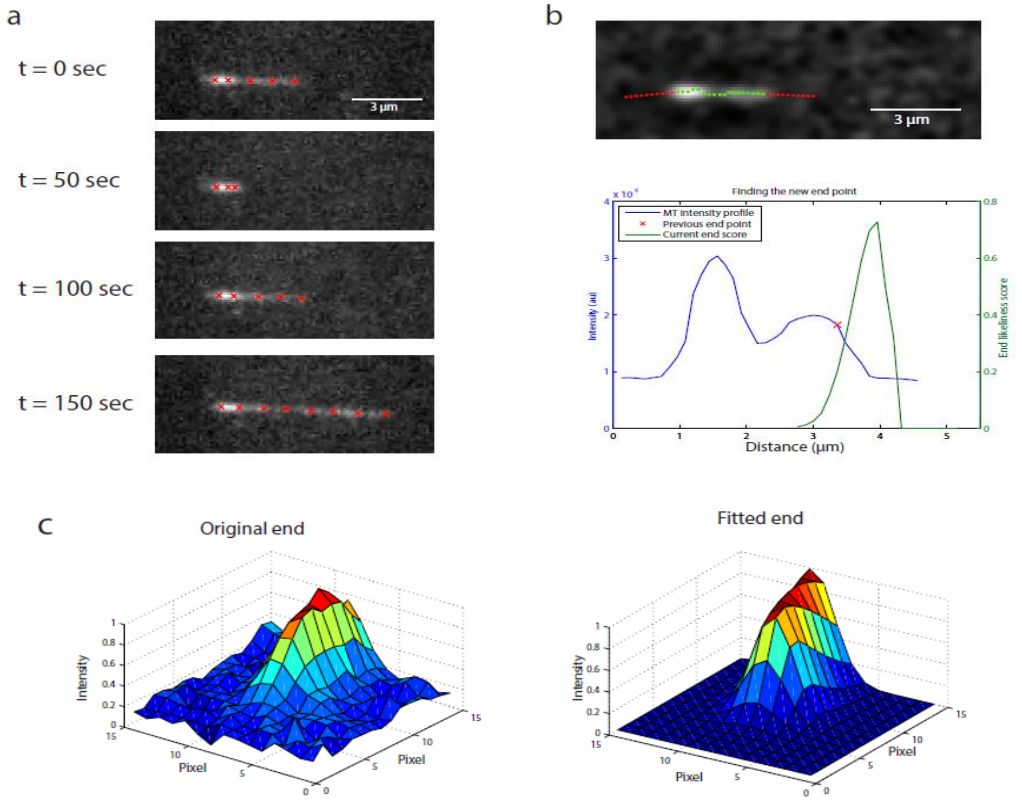

Figure 4: Microtubule Dynamics Analysis tracking procedure. *a) The principal of MT end tracking is to provide a space-time trajectory of the MT end position describing the history of the MT dynamics. b) Axial intensity profiles are used as evidence in a Bayesian prediction of the subsequent end position. This reduces the search area of the fitting function considerably improving the likelihood of fitting the end of the MT as opposed to noise. c)In contrast to some other methods, MDA uses 2D model fitting of the MT end. Figure provided by G. Bohner, personal communication.*

A Bayesian framework is then used with a prior constructed from the previously tracked positions and an assumption of the MT growth distribution. The new, rough end position is defined by the maximum of the posterior distribution computed by the convolution of the prior with a 1D intensity profile along the axis of the MT. Data from a number of frames before and after the current frame are used to dynamically switch the prior between a polymerisation model and a depolymerisation model accounting for the transient loss of MT signal in individual frames due to noise or defocussing.

Having determined a rough position of the microtubule, this is then passed as an initial guess to the two-dimensional fitting procedure described by Ruhnow et. al., 2011[21]. This two dimensional fitting procedure returns the end position defined in the 1D analogue as the mean of the Gaussian survival function fit to the axial end profile and the mean of a Gaussian fit to the lateral end profile.

1.3 Mean Square Displacement Analysis

The automated tip tracking methods presented above provide the large amounts of data required to build a statistical description of the inherently stochastic MT dynamics. In order to extract estimates for assembly kinetics such as the subunit association and dissociation rate constants, k_+ and k_- respectively, a model for MT polymerisation is required.

1.3.1 1D Growth Model

To estimate k_+ and k_- the commonly used model for fitting MT dynamics data to is a linear one-dimensional (1D) model[54]. This model assumes the MT can be characterised by a single discrete random variable $N(t)$ equal to the total number of tubulin subunits at time t. The addition and loss of tubulin subunits to the MT can be treated as a Markov chain in which time is continuous. The assumption is made that tubulin subunit addition occurs at a rate proportional to concentration, $k_+[\mathrm{Tub}]$, and tubulin subunit loss occurs at a constant rate, k_-, where $[\dots]$ indicates a concentration. Sample paths for $N(t)$ can be simulated using the Monte Carlo method (Section 2.2.2, Appendix 7A) a large number of which can be summed over to determine the model statistics, however for a simple 1D model these can be determined analytically.

1.3.2 Growth Model Statistics

In time δt the number of subunits additions is Poisson distributed with mean and variance $k_+[\mathrm{Tub}]\delta t$ and the number of subunit losses is Poisson distributed with mean and variance $k_-\delta t$. It follows from the properties of the Skellam distribution[55] that the mean change in $N(t)$ in time δt is given by Equation 1 and the variance is given by Equation 2.

$$\langle \delta N \rangle = (k_+[\mathrm{Tub}] - k_-)\delta t, \qquad 1$$

$$\sigma_N^2 = (k_+[\mathrm{Tub}] + k_-)\delta t, \quad 2$$

where $\langle \dots \rangle$ denotes the mean. Given l_{tub} is the length change contributed by a single subunit, on average 0.615nm, the mean growth velocity is

$$\langle v_g \rangle = \frac{\langle \delta L \rangle}{\delta t} = l_{tub}(k_+[\mathrm{Tub}] - k_-). \quad 3$$

Additional information about the kinetics is found in the variation of the length about its mean value which is proportional to time and defines an effective diffusion, D_{eff}, Equation 4 and 5[56].

$$Var[\delta L] = \langle \delta L^2 \rangle - \langle \delta L \rangle^2 = l_{tub}^2(k_+[\mathrm{Tub}] + k_-)\delta t = 2D_{\mathrm{eff}}\delta t \quad 4$$

$$D_{\mathrm{eff}} = \frac{l_{tub}^2}{2}(k_+[\mathrm{Tub}] + k_-) \quad 5$$

Many studies have estimated rate constants k_+ and k_- by recording data for the mean growth velocity at various tubulin concentrations and fitting the gradient and intercept to equation 3. These studies are summarised in Appendix 7C, however Gardner et al. (2011) have reported that not using the additional information in the variance of the length changes has led to an order of magnitude underestimation of the rate constants[19].

1.3.3 Mean Square Displacement

Displacements, or lengths, are measured by experiment at discrete time intervals with the possibilities limited to multiples of Δt, the inverse of the frame rate (fps). Considering a set $\{L_k\}$ of N successively recorded MT lengths, there are $N(N+1)/2$ non trivial forward displacements,

$$\delta_{ij} = L_j - L_i, 1 \le i < j \le N, \quad 6$$

$$\Delta t_{ij} = (j-i)\Delta t \quad 7$$

The most common definition of an estimator for MSD makes use of all possible displacements for a given multiple of Δt. Using this method however results in a highly correlated data set complicating theoretical calculations. Using, for example, the maximum number of nonoverlapping displacements of duration $n\Delta t$ for $n = 1, \dots, N-1$, we have

$$\langle \Delta L(n\Delta t)^2 \rangle = \rho_n = \frac{1}{\lfloor N/n \rfloor} \sum_{i=1}^{\lfloor N/n \rfloor} \delta_{i(i+n)}^2 \quad 8$$

where $\lfloor \dots \rfloor$ denotes the floor/integer part. This method is a compromise since the use of fewer data points at large n results in a noisier MSD estimator but all correlations between displacements are eliminated[23].

The 1D model statistics $\langle v_g \rangle$ and D_{eff} can be used to provide a theoretical description of the MSD, Equation 9, where σ_{err}^2 is the variance of the localisation precision[19,23–25].

$$\langle \Delta L^2 \rangle = \langle v_g \rangle^2 \delta t^2 + 2D_{\text{eff}} \delta t + 2\sigma_{\text{err}}^2 \qquad 9$$

This can be proved as follows. Consider the *displacement* of the MT tip, in time δt, to be normally distributed,

$$\Delta L \sim \mathcal{N}(\langle v_g \rangle \delta t, 2D\delta t) \qquad 10$$

with mean given by Equation 3 and variance given by Equation 4. The distribution of measured displacements will be the sum of the true distribution, ΔL and the distribution of measurement errors, δ_{err}. In the ideal case, errors have zero mean and are normally distributed with variance σ_{err}^2. Since two measurements, $\mathrm{m1}$ and $\mathrm{m2}$, are made in the determination of the displacement, the *measured* length change, which is distinguished in notation via a tilde, is given by,

$$\widetilde{\Delta L} = \Delta L(\delta t) + \delta_{\text{err}}^{(\mathrm{m1})} + \delta_{\text{err}}^{(\mathrm{m2})} \qquad 11$$

which is normally distributed,

$$\widetilde{\Delta L} \sim \mathcal{N}(\langle v_g \rangle \delta t, 2D\delta t + 2\sigma_{\text{err}}^2) \qquad 12$$

From the definition of variance, we have

$$Var\left[\widetilde{\Delta L}\right] = \langle \widetilde{\Delta L^2} \rangle - \langle \widetilde{\Delta L} \rangle^2 = 2D\delta t + 2\sigma_{\text{err}}^2 \qquad 13$$

which, using Equation 3, yields the mean square displacement as per Equation 9. This formulation however fails to take account of the fact that the camera is operated with a finite exposure time, effectively averaging over multiple end positions at each measurement.

1.3.4 Towards a 2D Model

The 1D model concerns itself with the length of the MT but does not consider the lengths of the individual protofilaments nor how the tip structure will affect $k_{\text{pf+}}$ and $k_{\text{pf}-}$, the local protofilament specific association and dissociation rates. 2D and 3D models have been used to show that there are indeed structural dependences leading to differences in $k_{\text{pf+}}$ and $k_{\text{pf}-}$. These include steric hindrances which reduce $k_{\text{pf+}}$ of lagging PFs[29,41] and increased $k_{\text{pf}-}$ due to fewer lateral bonds on leading PFs[19]. It has also been reported that the 1D model assumption that k_- is constant with respect to tubulin concentration is thermodynamically untenable for a multiple filament polymer[57]. Furthermore, there are predictions made by the 1D model which are not borne out by the experimental evidence such as concentration dependent taper length increases[58]. A Pseudo representation of taper length behaviour

can be introduced into the 1D model by random allocation of events (subunit additions and losses) to individual protofilaments and considering the lengths of protofilaments independently. This has limited practical value however as the average length of the protofilaments provides exactly the behaviour of the conventional 1D model while the taper length, defined as the difference in length of the longest and shortest protofilaments, is nothing other than a scaled description of the standard deviation of the 1D model, see Appendix 7A.

Although there are many problems with the 1D model, the predictions of more recent alternatives[19,59,60] are still analysed by fitting the statistics $\langle v_g \rangle$ and D_{eff} calculated from the 1D model to the MSD of MT ends. This is valid if the assumption is made that any complex dependencies k_+ and k_- may have on [Tub] and the taper structure are independent of time and MT length. This assumption allows Equation 1 and 2 to be written

$$\langle \delta N \rangle = (k_+^* - k_-^*)\delta t, \qquad 14$$

$$\sigma_N^2 = (k_+^* + k_-^*)\delta t, \qquad 15$$

where k_+^* and k_-^* are the time and length invariant global MT on and off rates for which Equation 9 will provide a valid estimate.

2 Methods

2.1 Tracking Accuracy

2.1.1 Rational

The accuracy and precision of the MDA tracking algorithm was determined using simulated data designed to reproduce, as accurately as possible, the data obtained via the experiments outlined in the Experimental Methods (1.2.1). It is important to point out that the aim of simulating TIRF microscopy data is to produce a "ground truth" to which tip location can be compared, not to realistically simulate the dynamics of the MT. There are a large number of parameters which may contribute to errors in determining the tip location which will need to be modelled independently of each other in order to determine their individual contributions to the accuracy of tip localisation. Furthermore, the combined effect of subsets of the individual error sources must also be understood in order to allow future experimental designs which minimise the combined tip localisation error as not all parameters can be independently controlled by the experimental design.

The principal source of error is expected to arise from two constraints. Firstly, the poor SNR in the dynamic MT TIRF data caused by the labelled free tubulin in solution and use of low, labelled to unlabelled tubulin ratios resulting in only partial decoration of the MT lattice with fluorescent

molecules. This tip structure may also play an important role as the tapered protofilaments result in a decreasing density of tubulin at the tip creating a local decrease in the SNR. Another possible source of error, largely ignored in previous analysis of tip localisation is the finite exposure time of the camera, which averages the tip position over time, effectively causing an asymmetric broadening of the PSF. Other parameters, including; growth velocity, fluctuations in growth velocity, lateral deflection of the MT, the orientation of the MT, the location of the tip relative to the image pixels, the pixel size and the PSF size may also be sources of error and it will be important to confirm if they have an effect on the tip localisation accuracy in the context of those sources discussed above.

2.1.2 Image Simulation

The simulation of time lapse fluorescence microscopy data of 13 protofilament, dynamic MTs was performed in MATLAB using a modification of the "model-convolution" approach[20,22]. This previous approach simulated static MTs by the convolution of a high resolution representation of the MT and binning into larger pixels equivalent to the projection onto the camera pixel grid. The modified method we have called "Gaussian-rendering", enabled the direct rendering of the larger pixels with the resulting speed up allowing the simulation of the large number of frames required to achieve statistical significance across the highly dimensional parameter set for dynamic MTs discussed above (section 2.1.1). The overall approach (**Figure 5**), was as follows: (1) for each frame, the number of subunits in all protofilaments was defined, (2) subunits were attributed a binary labelled/not labelled state, (3) the [x, y] coordinates of labelled subunits were defined within each image frame, (4) each frame was rendered by drawing a Gaussian approximation to the microscope PSF at each [x, y] coordinate of a labelled subunit, (5) frames were added to empty regions in real data or noise was simulated.

The details of the approach were as follows. First, the change in the total number of subunits in the MT in the time between acquired frames, Δt, was determined from a random sample of a Skellam distribution with mean defined by Equation 14 and variance defined by Equation 15[19,54]. In order to control for the effect of differing MT tip structures, the number of subunits in each protofilament was updated sequentially until all subunits had been added/lost. This maintains, on average, a specified linear distribution of protofilament lengths with width equal to MT tip taper length which would otherwise increase as the square root of time in an independent PF model (Appendix 7A). This was done not only to maintain an end structure that can be controlled for, but because it is not known how the additions should be distributed between PFs (Section 1.3.4) and should not affect determination of the parameter of interest, the end position. Next, each subunit in the first frame was randomly characterised as labelled or unlabelled, with probability of being labelled equal to the labelling ratio. Any additional subunits in subsequent frames were similarly characterised as labelled

or unlabelled however those subunits present in the previous frame maintained their labelling state. The [x, y] coordinates of the labelled subunits were then determined for each frame using the 3 start, B lattice model with radius 25nm and α-β tubulin subunit length 8nm (**Figure 5**a). The position lateral to the MT axis was then modified in each frame using a 1st order, uniformly loaded, cantilever beam model with normally distributed random tip deflection. The entire coordinate set was rotated and translated to position the MT in the desired location within the image frame.

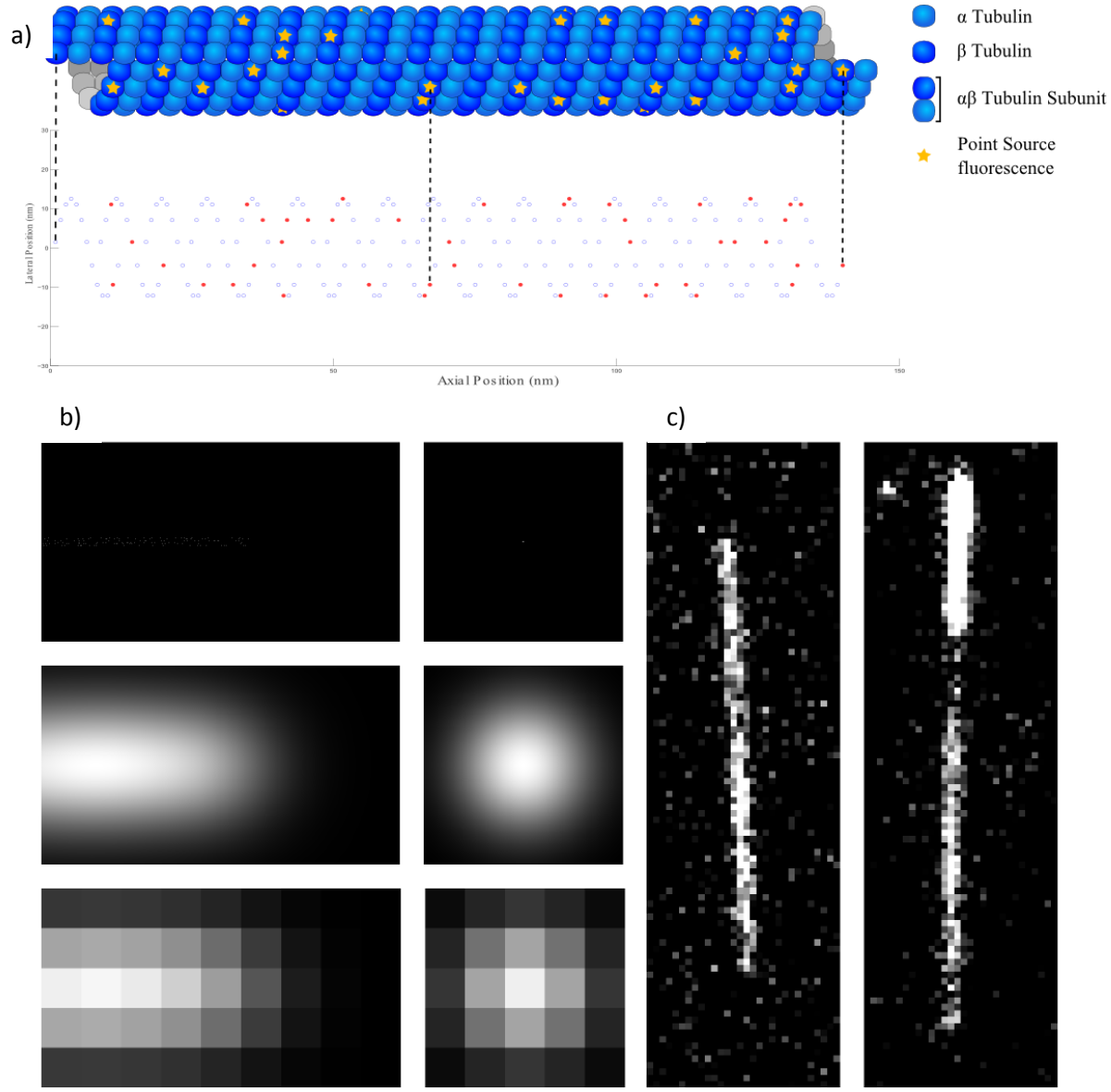

Figure 5: Simulation of TIRF microscopy of dynamic microtubules in vitro. *a) Schematic representation of the assumed 3D structure of the MT illustrating the random labelling of subunits and there projection onto a 2d plane such that there position can be mapped into an image. b) (Centre) a single centrally located point source equivalent to a δ function is imaged by a microscope. The light that falls onto the camera can be approximated to the first order by a Gaussian. This Gaussian is then downsampled by the discrete geometry of the camera pixels. (Left) The same process occurs for a collection of point. The structure of the light illuminating the cameral is a sum of the Gaussian contributions from each point source. c) (Centre) A simulated MT for comparison with (Left) a TIRF microscopy image of an MT.*

The final steps of the simulation render the image sequence in a manner appropriate for the specific imaging system used. First, all labelled subunits are considered point sources. Since the response of an imaging system to a point source, the PSF, can be approximated by a 2D Gaussian, a noiseless image can be rendered by calculating, for each pixel, the sum of the contributions of 2D Gaussians centred on each point source. This provides a "snap shot" of a single state of the MT. In reality there is a finite exposure time $t_E < \Delta t$ in which subunits are added and lost from the MT. Sub steps of individual subunit addition were not directly simulated but accounted for during rendering by a reduction in the peak intensity of the Gaussian contribution from subunits added during t_E. The proportion of t_E for which arriving and departing subunits were present in the MT lattice was approximated by a piecewise linear function. For example, during a growth episode in which n subunits were added during t_E this function is equal to 1 for subunits at a distance greater than n from the final end position and 0 for subunits at the end position. The intensity of these transient subunits was assumed to be directly proportional to the fraction of t_E they were present in the MT lattice. The noiseless image was multiplied by a constant factor in order to match experimental intensity values and non-zero mean Gaussian noise was added to the images to simulate the combination of the free tubulin background intensity and EMCCD camera noise. Alternatively intensity matched noiseless MT images were added to experimental images devoid of MTs.

It is necessary at this point to distinguish between the *real* end position, the *visible* end position and the *measured* end position. There are significant differences between the three values because of typically low experimental labelling ratios and localisation uncertainty.

We will denote the measured position with a tilde, the visible position with a breve and the true end position without. For instance, an MT with a real end position at time t will be notated, $\vec{\boldsymbol{r}}(t) = [x(t), y(t)]$, whereas its visible and measured end positions will be noted $\breve{\vec{\boldsymbol{r}}}(t) = [\breve{x}(t), \breve{y}(t)]$ and $\tilde{\vec{\boldsymbol{r}}}(t) = [\tilde{x}(t), \tilde{y}(t)]$ respectively. The real end position $\vec{\boldsymbol{r}}(t)$ is unknown in the experimental data but is defined in the simulation as the mean of the coordinates of the final subunit on each of the 13 protofilaments $[\bar{x}(t), \bar{y}(t)]$, independent of labelling state or taper structure. The visible end position $\breve{\vec{r}}(t)$ is the available data to which the tracking program localises the end and is defined in the simulation as the mean of the real $[\bar{x}(t), \bar{y}(t)]$ coordinates of the labelled subunit on each of the 13 protofilaments which were added during t_E. The measured end position $\tilde{\vec{\boldsymbol{r}}}(t)$ given by the tracking program is the sum of the visible end position and some localisation error. These definitions of end position are arbitrary in the sense that they define a specific point of reference within a region of the MT which has a broad characterisation in terms of dynamics, function and structure. They are relevant

points of reference when considering both the imaging system and the tracking algorithm however and their choice is justified in section 3.1.1.

2.1.3 Accuracy and Precision

The accuracy and precision of the MDA tracking algorithm was determined by tracking simulated MTs with coverage of the parameter set achieved first by single parameter variations from an ideal set for which accuracy and precision are assumed to be optimal. Secondly, significant parameters were varied in a pairwise manor in order to identify interactions. Finally, a subset of parameters constrained by experimental considerations was used to confirm the identification of explanatory variables.

The primary output of MDA is an $\tilde{\vec{r}}(t) = [\tilde{x}(t), \tilde{y}(t)]$ coordinate estimating the end position of the MT in the image space for each frame. The norm vectors tangent and normal to the MT are determined from the simulation output and the measured end position was projected onto this coordinate system such that the difference $\widetilde{\overrightarrow{\boldsymbol{r}_{\mathrm{MT}}}}(t) - \overrightarrow{\boldsymbol{r}_{\mathrm{MT}}}(t)$ gave the absolute error $\vec{\boldsymbol{\varepsilon}}(t)$ which can be decomposed into its axial, $\mathcal{E}_A(t)$, and lateral, $\mathcal{E}_L(t)$, componants.

For every parameter set a minimum of 15 data sets (movies) were simulated each with a minimum of 50 frames giving $N = 750$ data points from which $\vec{\boldsymbol{\varepsilon}}(t)$ was calculated. Accuracy and precision were defined as the mean and standard deviation of $\vec{\boldsymbol{\varepsilon}}(t)$ respectively,

$$\overrightarrow{\boldsymbol{\mu}_{\varepsilon}} = \frac{1}{N}\sum_{i=1}^{N} \vec{\boldsymbol{\varepsilon}}_i(t), \tag{16}$$

$$\overrightarrow{\boldsymbol{\sigma}_{\varepsilon}} = \sqrt{\frac{1}{N-1}\sum_{i=1}^{N} \left(\vec{\boldsymbol{\varepsilon}}_i(t) - \overrightarrow{\boldsymbol{\mu}_{\varepsilon}}\right)}. \tag{17}$$

A bootstrapping and bagging procedure[61] was used to provide an estimate for the error on these values. This was done by taking $m = 15$ subsets of $n = 50$ data points, sampled at random with replacement from the total N data points, m estimates of the mean and standard deviation could be made from these subsets. The standard error on $\overrightarrow{\boldsymbol{\mu}_{\varepsilon}}$ was then calculated as follows,

$$SE_{\mu} = \frac{1}{\sqrt{m}} \sqrt{\frac{1}{m-1}\sum_{j=1}^{m} \left(\mu_{\varepsilon}^{(j)} - \overline{\mu_{\varepsilon}^{(m)}}\right)}, \tag{18}$$

where vector notation has been dropped for simplicity. Equation 18 was also used with the $\sigma_{\varepsilon}^{(m)}$ estimates of standard deviation to calculate the standard error, SE_{σ}, on $\overrightarrow{\boldsymbol{\sigma}_{\varepsilon}}$.

2.2 Mean Square Displacement Analysis

2.2.1 Rational

The value of MSD analysis lies in the relation of observed trajectories to underlying diffusion coefficients. This relation is not trivial however and a number of confounding factors such as finite resolution and exposure time integration of trajectories should be considered. The suitability of this analysis to determining the D_{eff} of 1D polymer growth is investigated using simulated MT growth data. It is important to note that for convenience a 1D model for which statistics $\langle v_g \rangle$ and D_{eff} are known (section 1.3) is used and that the question of whether this model can be applied to MT dynamics remains open.

2.2.2 MT Length Simulation

The continuous time MT length is simulated using a Monte Carlo[62] implementation of the 1D model (Section 1.3.1), see Appendix 7A and Fall et. al. (2005)[63]. Briefly, the 1D model is a continuous time, Markov chain so a sequence of micro-times $\{t_i\} = t_{i-1} + \mathcal{T}_i;\ i = 1,2,\ldots$ were computed by randomly sampling from the dwell time probability density function,

$$\mathcal{F}_{\mathcal{T}}(\tau) = (k_+ + k_-)\exp[-(k_+ + k_-)\tau] \qquad 19$$

where $\tau \in [0, \infty)$, is the time since the previous event[64,65]. This sequence of micro-times at which events (subunit loss or addition) have occurred can be used to simulate the number of subunits $N(t)$ at all times by performing the logical test

$$N(t \in [t_i, t_i + \mathcal{T}_{i+1}]) = \begin{cases} N(t_{i-1}) + 1 \leftrightarrow R_i < k_+/(k_+ + k_-) \\ N(t_{i-1}) - 1 \leftrightarrow R_i > k_+/(k_+ + k_-) \end{cases} \qquad 20$$

on a set of uniformly distributed random numbers $\{R_i\} \in [0,1]$.

The length of the MT is defined as $L(t) \equiv l_{tub}N(t)$ where l_{tub} is the length contributed by a single subunit, on average 0.615nm. The number of subunits in the MT was resampled from $N(t)$ at time intervals $\Delta t = 1/\mathrm{fps}$ to produce $N(k\Delta t);\ k = 1,2,\ldots$ the macro-time sequence used to determine the length of the MT in each frame. When sub steps were not required the macro-time sequence $N(k\Delta t)$ was calculated using a random sample from a Skellam distribution with mean defined by Equation 1 and variance defined by Equation 2 as per Section 2.1.2.

The effect of tip localisation error was simulated by adding a random variable $\delta_{\mathrm{err}} \sim \mathcal{N}(0, \sigma_{\mathrm{err}}^2)$ to $L(k\Delta t)$ in each frame[66]. The effect of camera exposure time was simulated by adding a random variable $\delta_{\mathrm{E}} \sim \mathcal{N}(-\langle v_g \rangle t_{\mathrm{E}}, 2Dt_{\mathrm{E}})$ to $L(k\Delta t)$ in each frame.

2.2.3 Mean Square Displacement Analysis

MSD estimators were calculated using a modified version of msdanalyser, a per-value MATLAB class written by Tarentino et. al., 2014[67]. This algorithm uses the more common form of the MSD estimator,

$$\langle \Delta L(n\Delta t)^2 \rangle = \rho_n = \frac{1}{N-n} \sum_{i=1}^{N-n} \delta^2_{i(i+n)},\ n = 1, \dots, N-1 \qquad 21$$

which makes use of all available displacements resulting in a correlated but less noisy MSD estimate. Each MT trajectory is used to produce a single, time averaged MSD curve from which a *mean* Mean Square Displacement curve can be calculated by taking the mean of all MT MSD curves at a given time delay. This mean is weighted by the number of time delays used to produce the initial MSD curves. A weighted standard deviation was also be calculated. There is no consensus with regard to defining a confidence of a weighted mean so for illustrative purposes a standard error was defined as,

$$SE_{MSD} = \frac{\hat{\sigma}_{MSD}}{\sqrt{N}} \qquad 22$$

where $\hat{\sigma}_{MSD}$ is the weighted standard deviation and N is now the number of MT trajectories used in the ensemble average. Not that MSD can only provide an average behaviour, for trajectories which are formed of multiple diffusive modes a single value for the diffusion coefficient will be returned by MSD analysis and it will be heavily biased towards the larger of the true diffusion coefficients that describe the trajectory[23].

3 Results

3.1 Model Verification

Prior to assessing the accuracy of MT end position localisation, a number of assumptions made in the simulation of the TIRF data needed to be verified.

3.1.1 End position

The definition of the real end position of the MT is arbitrary, to have meaning however it should be both consistent and relevant to the context in which it is used. In section 2.1.2 the visible end position was defined as the mean of the position of the labelled subunits added during the exposure time and the true end position was defined as the mean of the last labelled subunit on each of the protofilaments at the end of the exposure time. This assumption was verified in by construction of a 1D representation of an imaged MT as a sum of Gaussians with randomly positioned means at a density equal to the αl_{tub} where α is the labelling ratio. Tapered ends could then be simulated by defining a region of specified length over which the density was reduced linearly, representative of a

reduction in the number of subunits in the tapered structure. There are not multiple protofilaments in the 1D representation however an equivalent point exists. For the blunt end this is the centre of the last Gaussian on the MT. For a tapered end this is the point where the linear distribution of the Gaussian density, i.e. the middle of the taper distribution.

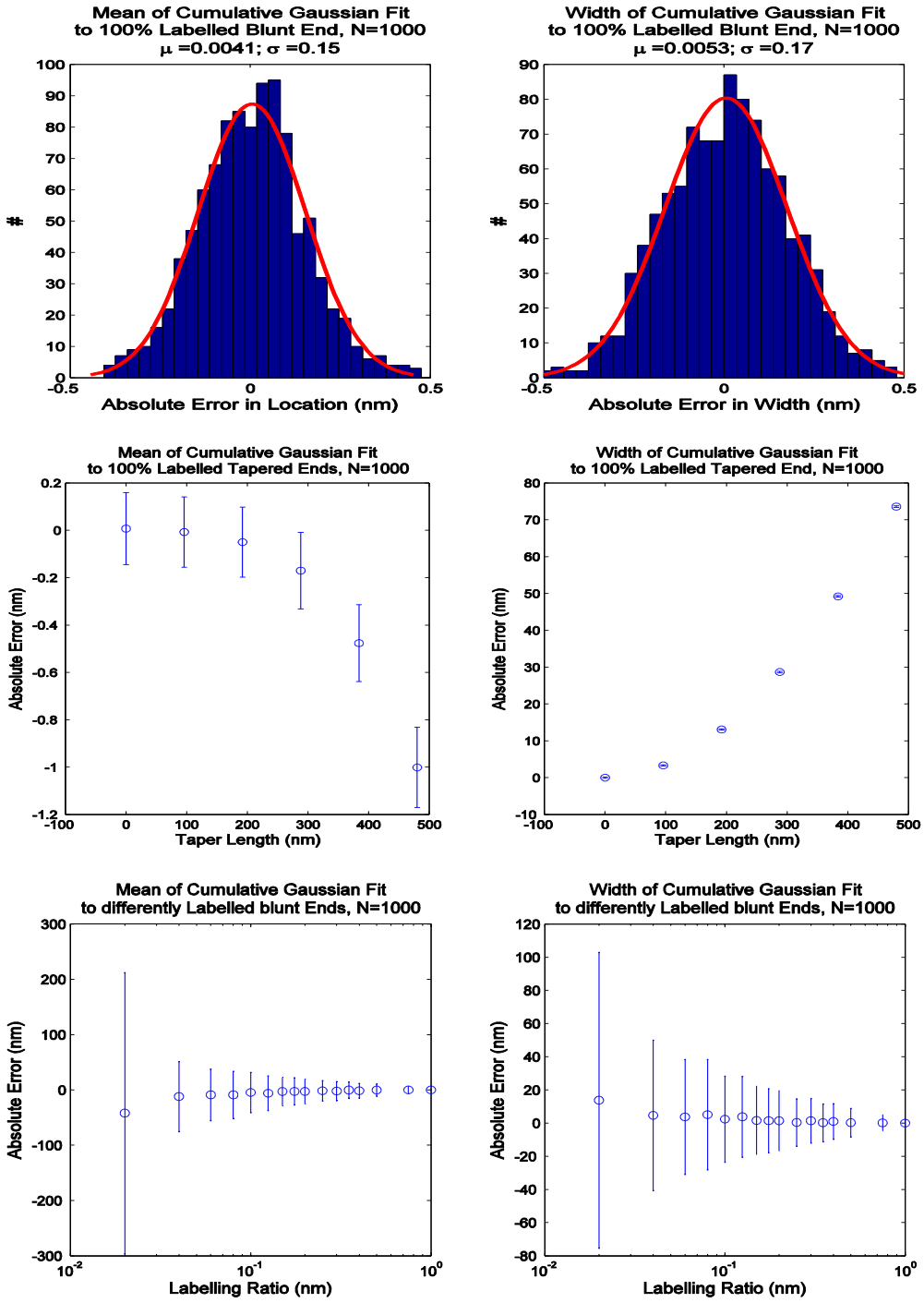

Figure 6: Cumulative Gaussian fits to 1D microtubules. *A Cumulative Gaussian was fit to a sum of Gaussians distributed randomly according to the density of labelled subunits. The difference between the mean of the cumulative Gaussian and the 1D MT end (defined in the text) is plotted against taper length and labelling ratio. Error bars are standard deviations. All data points are mean values for N=1000 fits to the end position of the 1D MT.*

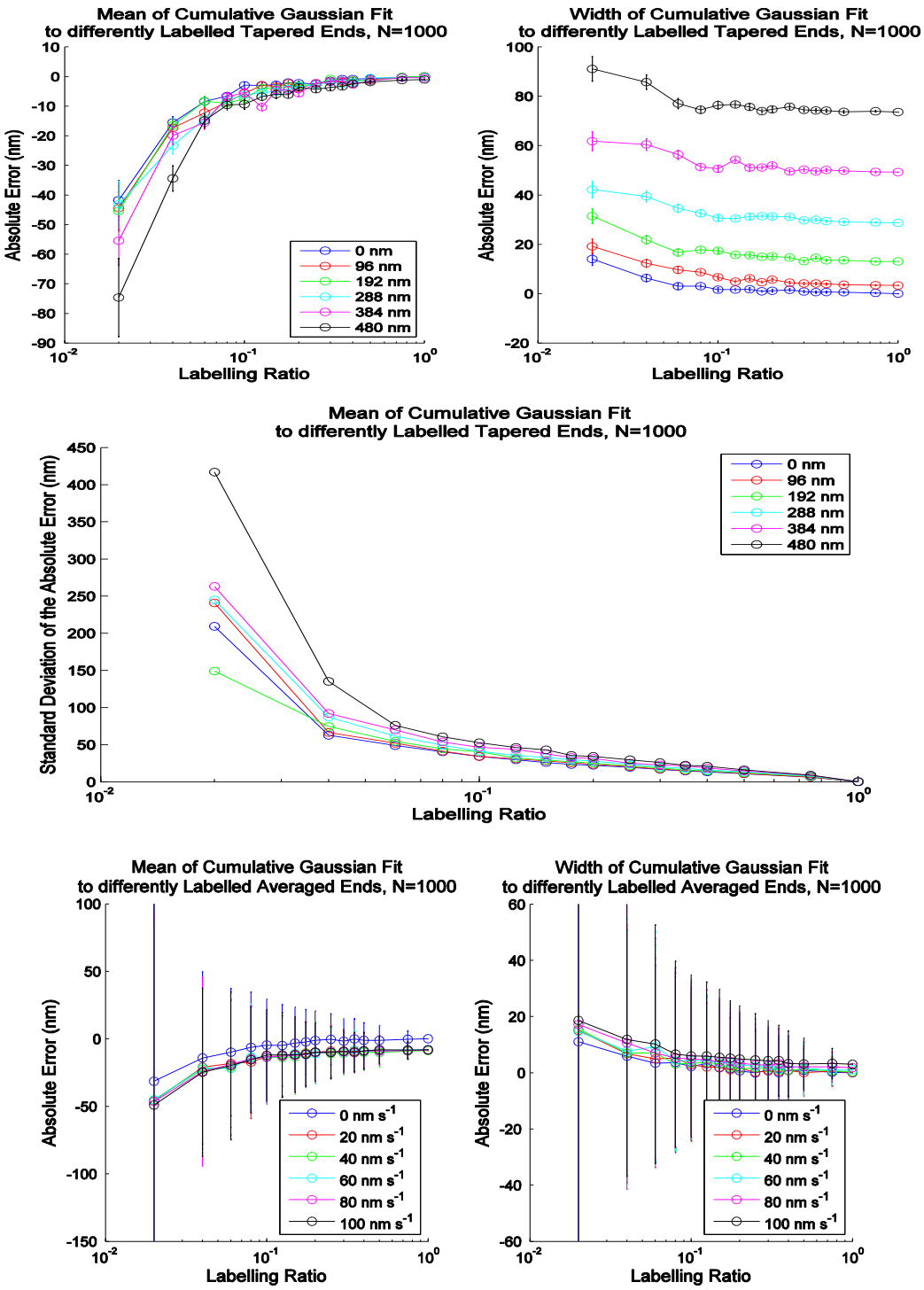

Figure 7: Cumulative Gaussian fits to differently labelled tapered and time averaged 1D microtubule ends. *The difference between the mean of the cumulative Gaussian and the 1D MT end (defined in the text) was plotted for both labelling ratio and taper length. The combined effect indicates the two factors independently influence the determination of the end position. This absolute error was also plotted against the average end position over a finite exposure time. Error bars on the top two graphs are standard errors. Error bars on the bottom two graphs are standard deviations. The central graph is the standard deviation of the absolute error in position for differently labelled tapered ends. All data points are mean values for N=1000 fits to the end position of the 1D MT.*

The absolute error in the determination of the end position, by this definition, was not more than 10nm (**Figure 6**, **Figure 7**) at relevant labelling ratios, $\alpha > 10\%$. It was also noted that the width of the cumulative Gaussian fit did increase significantly with taper length, however this effect was not linear as reported by Demchouk et. al., (2011)[20]. Camera exposure time was modelled not as a linear reduction in density but a linear reduction in the peak intensity of the Gaussian contribution from the region defined as growing or shrinking. It is expected from theory that this distribution of intensities should follow a cumulative exponential distribution for pure growth or pure decay since the dwell times are exponentially distributed (Appendix 7B). The combination of these effects would then follow a cumulative Laplacian distribution. This cumulative exponential is observed (**Figure 8**) when the substeps are simulated using a Monte Carlo simulation, (as is a cumulative Laplacian in the combined case, data not shown) however, it is clear by visual inspection alone that in the regime of MT kinetics these distributions can be very well approximated by a piece wise linear function. Intensity modulation of the end region Gaussians by the fractional exposure times shown in **Figure 8** are equally accurately localised by a cumulative Gaussian fit (data not shown) as the linear model used in **Figure 7**. This analysis confirms that the definition of the end position used is consistent across a range of relevant parameters. It was also noted that parameters included in this analysis act independently of one another to produce the observed total accuracies and precisions.

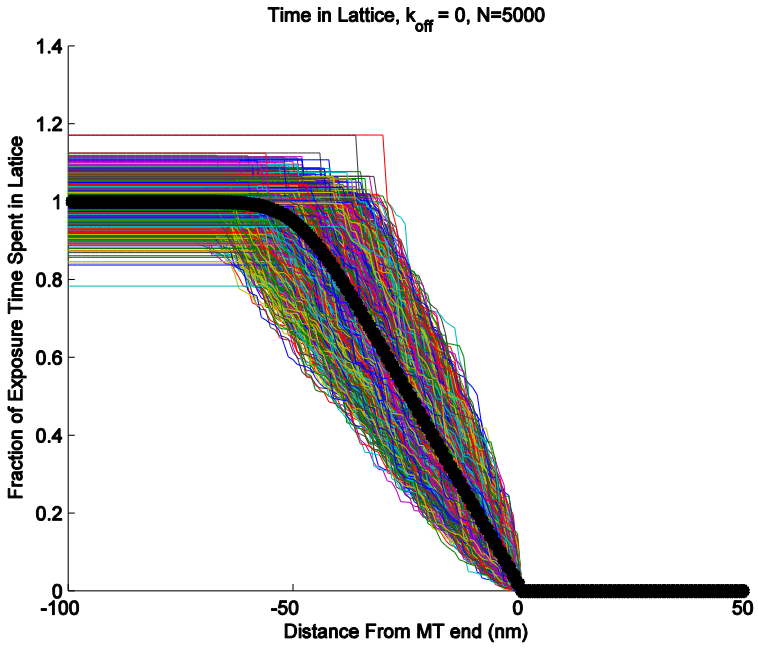

Figure 8: Time in frame of transient subunits in a 1D microtubule. *The cumulative time spent in the microtubule lattice during a 0.5s exposure as a fraction of the total exposure time, is plotted with the final subunits aligned. The mean of N=5000 growth episodes is shown in black. The growth was simulated using the 1D model (Section 1.3.1) with* $\langle v_g \rangle = 50\ nm\ s^{-1}$ *and* $k_- = 0$ *for simplicity. Non-unity values for lattice bound subunits is due to randomly distributed time steps in the simulation which do not necessarily sum to 1.*

3.1.2 Noise Simulation

In order to properly assess the effect of varying noise on the accuracy of tracking noise at different signal to noise ratios was simulated. It is important to verify however that the description of the noise used in the simulation accurately represents the true noise. The microscope uses an EMCCD camera which is characterised by its Poisson counting statistics[68]. These cameras are well characterised and there noise can be very well modelled by a Gaussian distributed random variable. The environment of the sample however contains a large number of freely diffusing fluorescently labelled tubulin molecules. This complicates the analytical determination of the noise. Instead the noise characteristics were determined empirically from MT free regions of real microscope data. The first and second moments of the noise suggest it is Gaussian distributed but does not confirm if there is pixel to pixel or frame to frame independence. To determine this a 3D auto-correlation of the noise from the data was calculated for 200 images across a 512x512 square region. A representative selection of this correlation for a single 100x100 pixel 2D plain is shown in **Figure 9**. The correlation function is approximately a Dirac Delta function suggesting independence, as expected from EMCCD noise superimposed on freely diffusing independent point sources. Long range correlations were occationally observed and can be attributed in the case of [x,y] space to the non-uniform illumination by the TIRF field and in time by variations in intensity. These correlations are small however and not spatially or temporally similar to the dimensions of the MT tip so independence can be assumed.

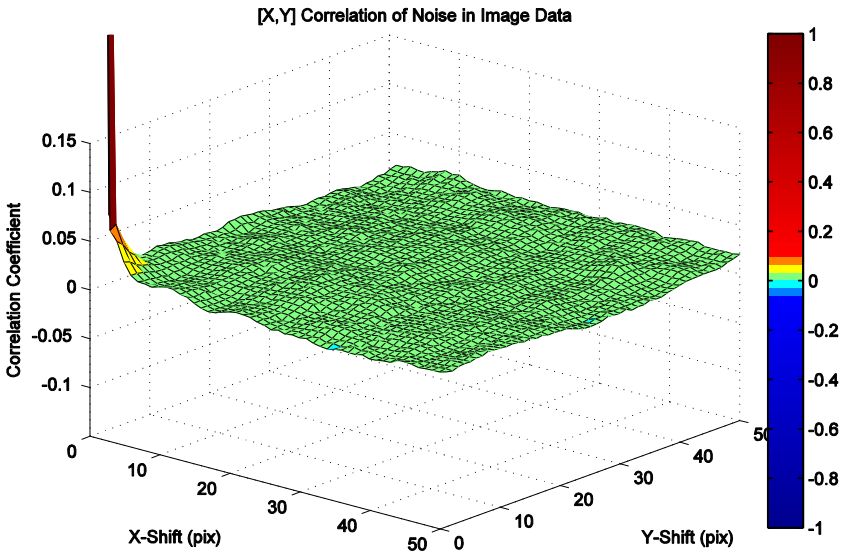

Figure 9: Noise Correlation in TIRF data. A 100x100 2D plane of noisy data was used to calculate this autocorrelation function. The correlation is zero across the entire plane and as such the noise can be considered independent.

3.2 Tracking Accuracy

3.2.1 Independent parameter variation

Tracking accuracy and precision as defined in Section 2.1.3 was calculated from 15 movies of 50 frames each. Parameters were first varied independently from a Best case scenario where the SNR is infinity, the microtubule is 100% labelled, there is no random movement in the MT tip position and the exposure time is 0s (a "snapshot" image of one state of the microtubule). Orientation and position with respect to the [x,y] pixel grid were controlled for by choosing a random orientation and a random [x,y] start position in each movie. Every parameter set that was used to form the following data sets can be found in Appendix 7D.

3.2.1.1 "Best Case" and spatial Dependences

The "Best Case" consists of 15 separate movies and 50 separate frames however each and every frame is identical with the end position stationary and well defined by virtue of 100% labelling and an infinite SNR (**Figure 10**).

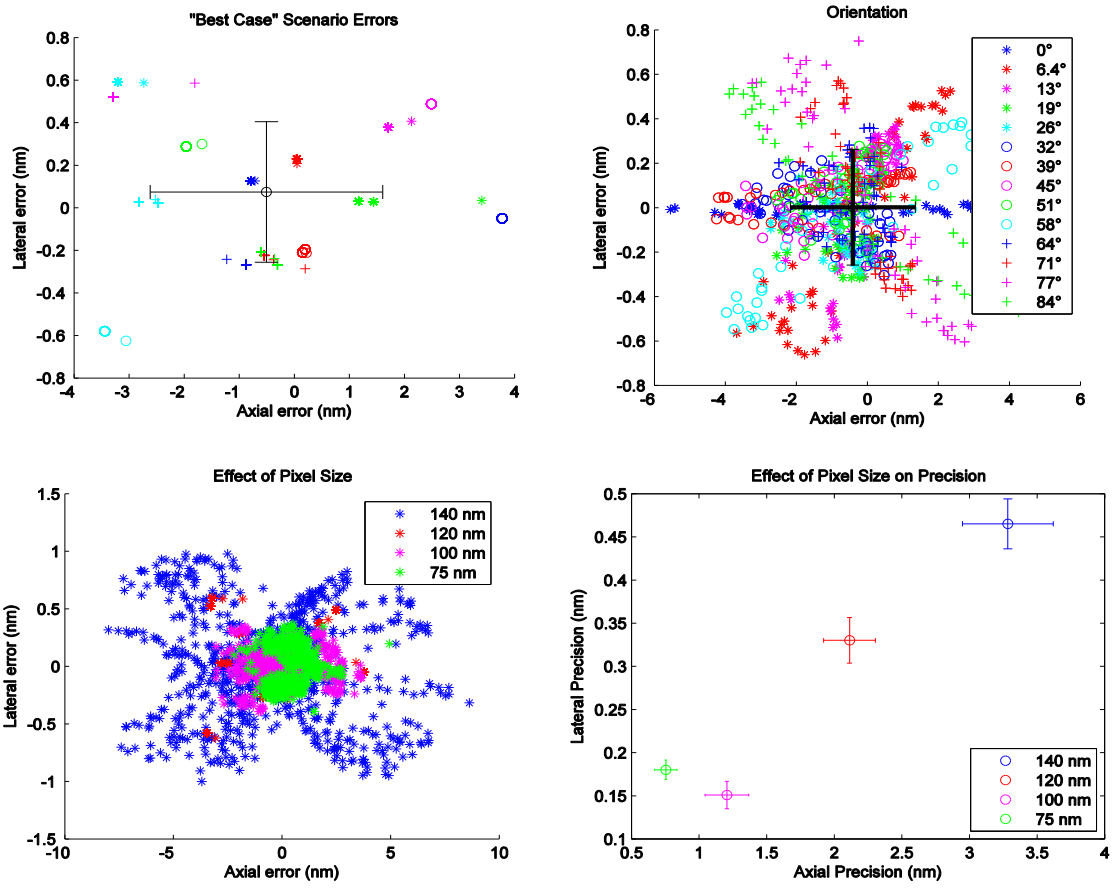

Figure 10: "Best Case" and associated spatial considerations. *(Top Left) The axial and lateral errors are plotted for every localisation (N=750) along with the mean (accuracy) for the "Best Case" senario. (Top Right, Bottom Left) The axial and lateral errors are plotted for differing orientations and pixel sizes. (Bottom Right) The Axial and lateral precision are plotted for various pixel sizes. Error Bars are standard errors.*

This “Best Case” represents a single source of error, that is the ability of the non-linear least squares fitting algorithm to fit the down sampled (pixilated) MT end. Differences between movies are likely to arise from the trajectory the curve fitting algorithm takes from the program users marking of the rough end position. With decreased tolerances the precision of the fitting can be reduced although there will be a lower bound to the accuracy inherent in the position of the MT end relative to the pixel grid. This change in precision can be seen clearly when the MT is rotated (**Figure 10**) or moved across the pixel grid (**Figure 11**). The size of the pixels also plays a role with larger pixels reducing precision. This is exactly analogous to the Nyquist frequency problem when sampling any continuous distribution.

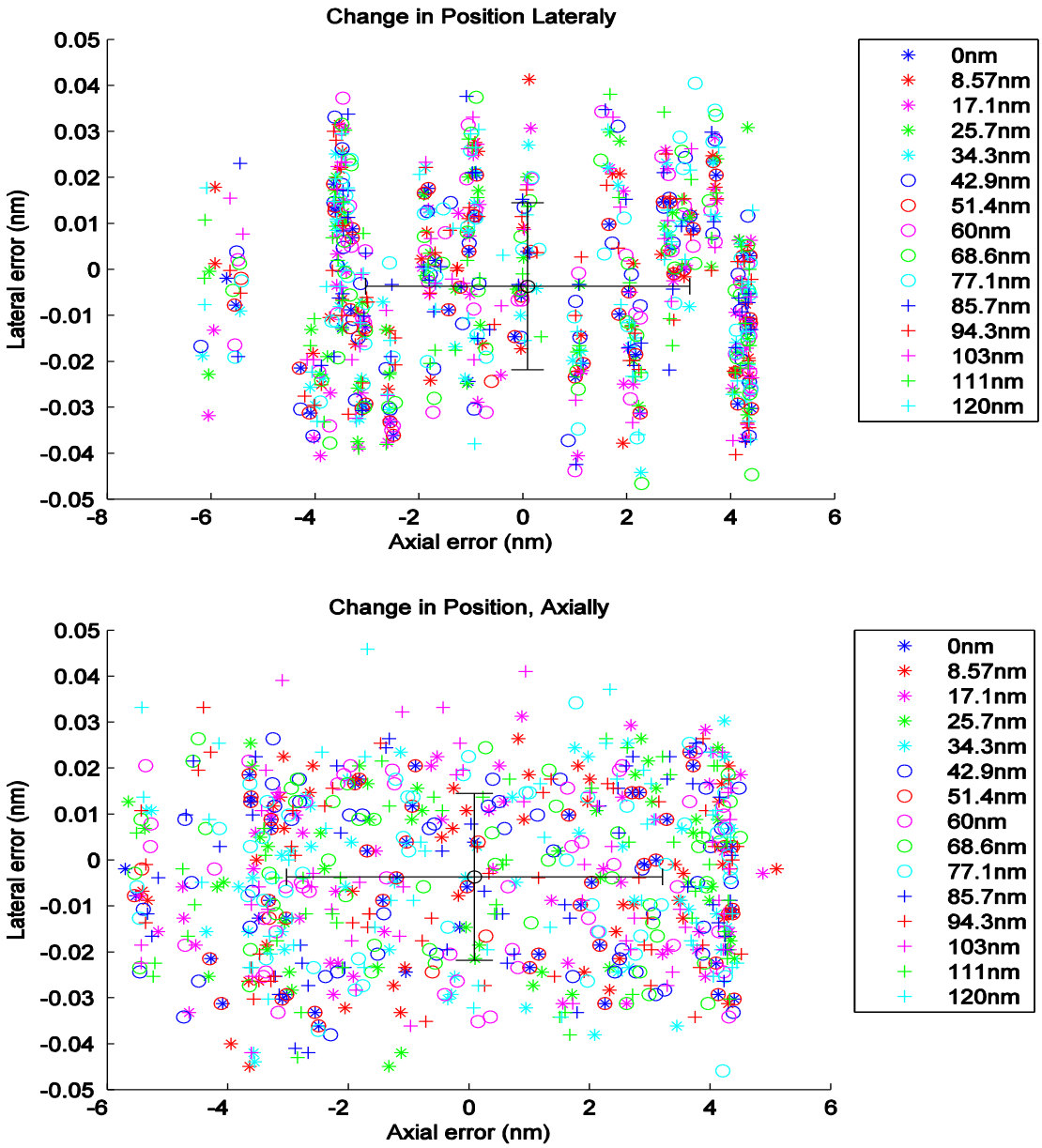

Figure 11: The effect of the position of the MT relative to the pixel grid. *The axial and lateral errors are plotted along with the accuracy for differing axial and lateral positions relative to the pixel grid. Error bar is standard Error.*

3.2.1.2 Tip Movement

It is critical for post analysis methods such as MSD analysis that there is no bias in the error preferential or detrimental to the recording of position changes. If this were the case the resulting output would correlated and much of the statistical framework behind the analysis techniques relies on independent identically distributed random errors. This appears to be the case with all forms of motion tested (linear growth, fluctuating growth and lateral deflection) exhibiting a normal distribution of errors with accuracy and precision as good as or better than that seen for the "Best Case". (**Figure 12**)

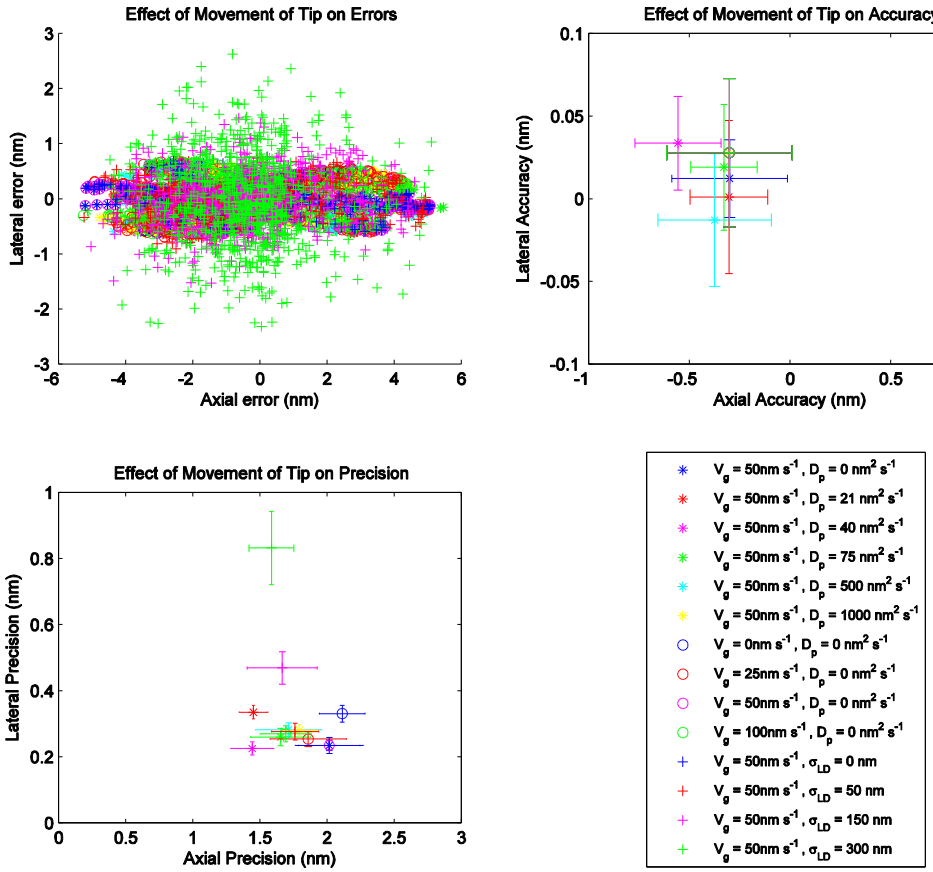

Figure 12: Effect of Movements in the MT end position*. The axial and lateral errors are plotted along with the accuracy for differing movements of the MT end position including slow to fast constant growth, small and large fluctuations in growth speed and lateral deflections. Error bars are standard Errors.*

3.2.1.3 Labelling Ratio

Since the fluorescent labelling of tubulin both disturbs MT dynamics at high ratios and leads to denaturing of a significant portion of the tubulin during preparation it is an important experimental consideration. It is observed that the labelling ratio is strongly correlated with precision, particularly in the axial direction (**Figure 13**). Conversely the accuracy appears to behave nonlinearly, remaining

very stable and close to zero until a threshold is reached at ≈ 0.15. Demchouk et. al. (2011)[20] have noted a similar nonlinearity in the labelling ratio's contribution to the SNR (not considered here because the SNR is controlled separately). This behaviour was also observed in the 1D representation used to confirm the definition of the end position however, in practice labelling ratios of > 0.15 are readily achievable and if due consideration for this effect is given by experimentalists it may be mitigated.

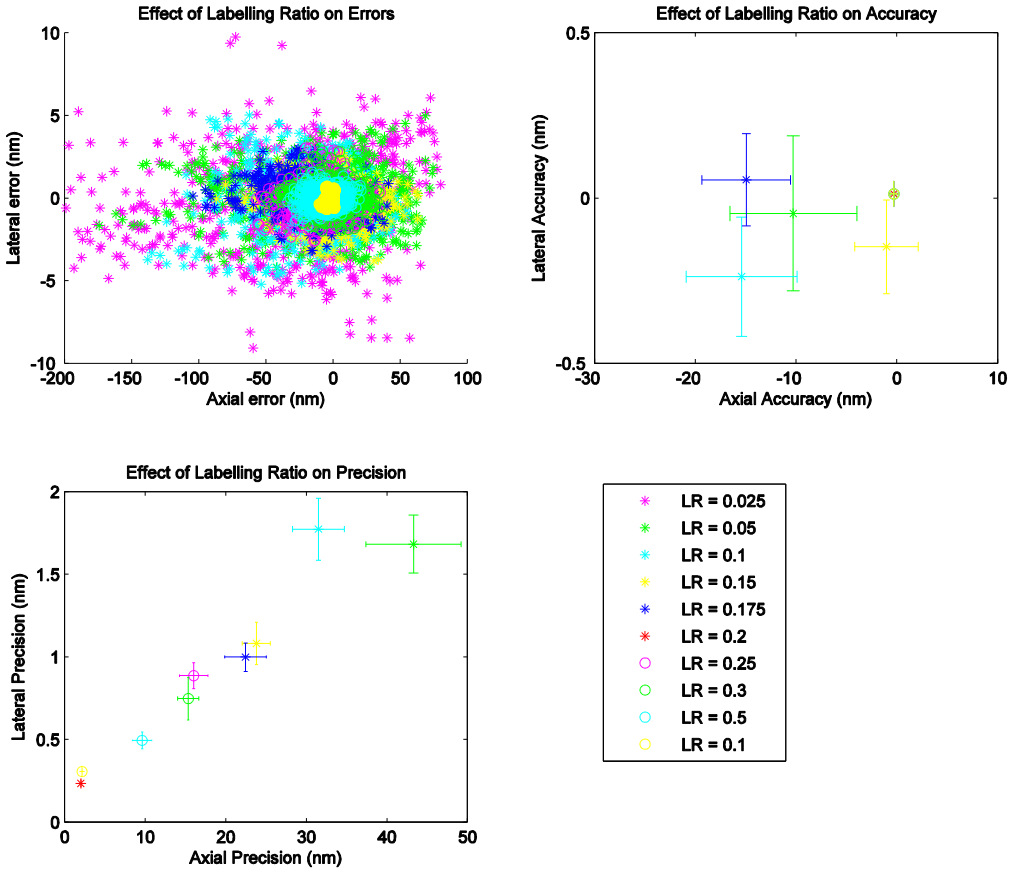

Figure 13: Effect of labelling ratio on tracking*. The axial and lateral errors are plotted along with the accuracy for differing labelling ratios. The precision is strongly correlated with the labeling ratio. Error bars are standard Errors.*

3.2.1.4 Signal to Noise

The signal to noise ratio was defined by three parameters which were controlled in the simulation, μ_{BG}, the mean background intensity, σ_{BG}, the standard deviation of the background intensity and μ_{MT}, the mean signal intensity. Both from the statistics of EMCCD photon counting and empirically from microscope data the variance of the background was varied proportionally to the mean background. Typical experimental levels for SNR are in the region of μ_{BG}=7000, σ_{BG}=500 and μ_{MT} = 9000. The end position estimates from the simulated data set with these parameters have a lateral precision of 38.75

(SE = 4.72) which is the largest, single parameter dependent, experimentally relevant value seen for any parameter. The errors are normally distributed however and the accuracy is small. The precision is however very strongly correlated with SNR (**Figure 14**).

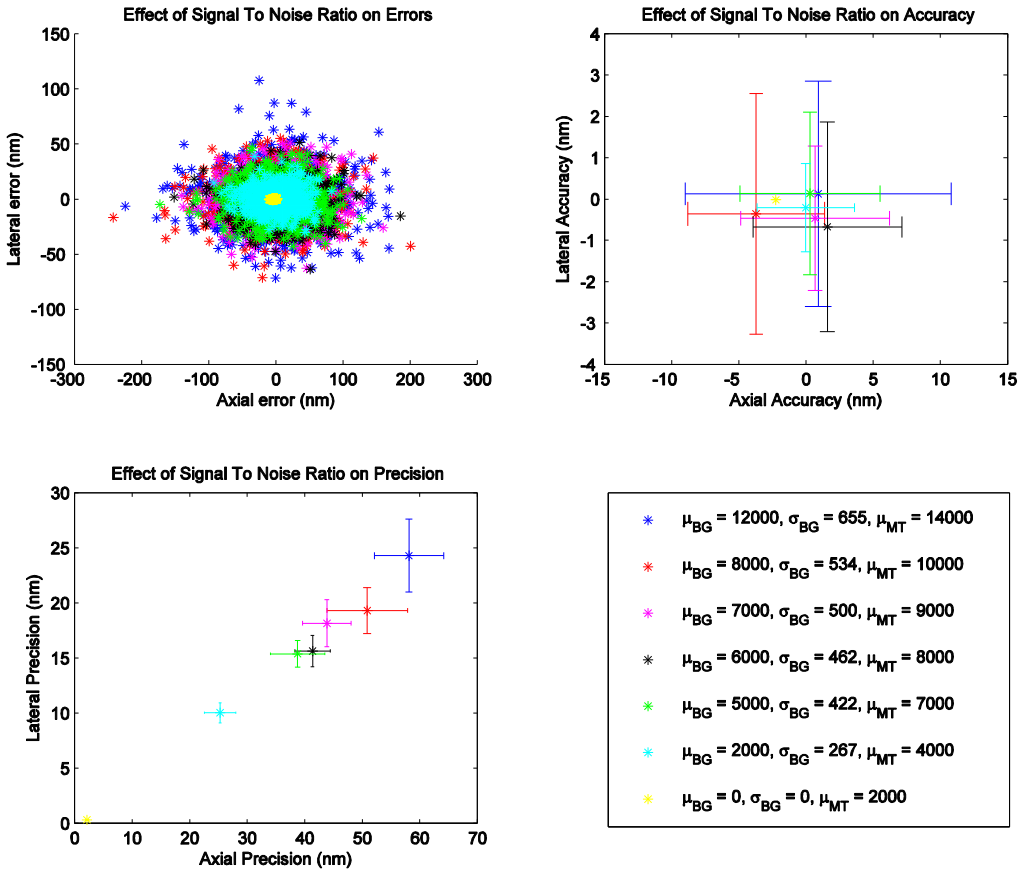

Figure 14: The effect of different SNRs on tracking. *The axial and lateral errors are plotted along with the accuracy for differing signal to noise ratios. The precision is strongly correlated with the SNR. Error bars are standard Errors*

3.2.1.5 Exposure Time and Taper Length

Even taking account for the exposure time in the definition of the end position a negative correlation was observed between the axial accuracy and the exposure time resulting in underestimates of the MT length. These changes are small though, even compared to the "Best Case" accuracies. Since the precision of the tip localisation is not changed it is likely that definition of the end is not rigorous enough to completely remove the large biases in accuracy seen when only considering the last point in the exposure **Figure 15**. Unexpectedly the taper length shows a small positive bias in the accuracy at longer taper lengths **Figure 15**. It is possible that weighting given to the width of the error function under the default settings in MDA is partially responsible for the less accurate fit. It is possible to change these settings although this was not done here.

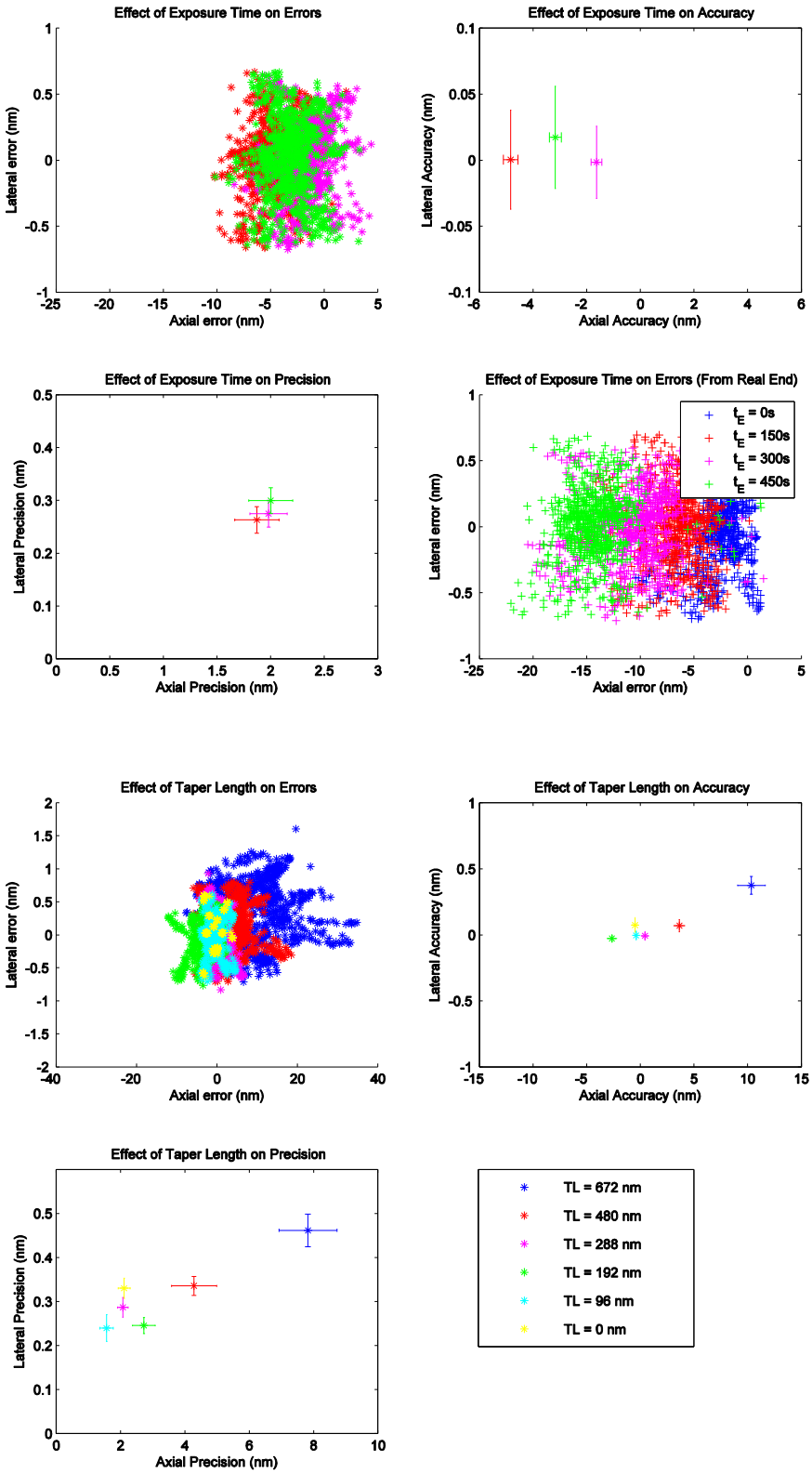

***Figure 15: Effect of exposure time and taper length on tracking**. (Top Row) Errors and accuracy at varying exposure times. (Second Row) The precision at various exposure times and the errors when only the final MT state in the exposure time is considered the end position. (Third Row) The errors and accuracy at various taper lengths. (Bottom Row) The precision at various taper lengths. Error bars are standard errors.*

3.2.2 Parameter Covariance

It was considered possible that increasing SNR, or decreasing labelling ratio would significantly affect the tracking accuracy in cases such as long taper lengths and long exposure times where an extended, sparsely labelled, or weak intensity tip would be obscured by noise resulting in negative biases. This was not the case however (Data not shown, see Appendix 7D). As per the 1D representation combining taper length, exposure time and labelling ratios did not produce changes in accuracy or precision that could not be explained by the independent combination of the three parameters.

The most significant errors in the independent parameter variations were the labelling ratio and the SNR. The combined effect of these two variables is shown in **Figure 16**. The accuracy of the combined effect is still not significantly different from zero however the precision reveals the dominance of the effect caused by the SNR ratio.

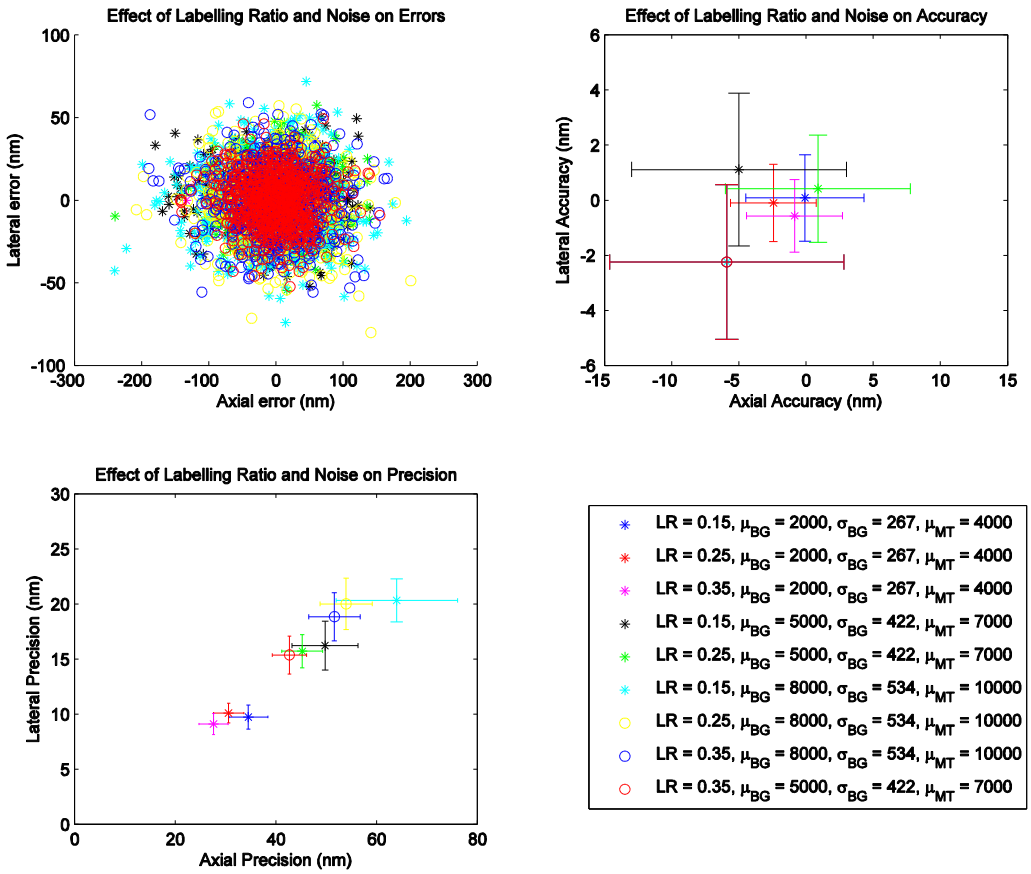

Figure 16: Combined effect of labelling ratio and SNR. *The axial and lateral errors are plotted along with the accuracy for differing labelling ratios and signal to noise ratios. The precision is again strongly correlated with the SNR.There is a less significant correlation with the labelling ratio however resulting in three distinct clusters. Error bars are standard Errors*

In **Figure 16** nine test data sets are shown which take three different values of SNRs and three different labelling ratios at each SNR. The result is three clusters stemming from the primary correlation being with the SNR and within these clusters the data sets with the lowest labelling ratios have larger axial precision as per the independent variation of labelling ratio.

This effect is seen again in the simulation of data sets with experimentally relevant parameters (**Figure 17**) (Appendix 7D). Here, two different values of SNR were used and three other parameters varied, the most significant of which (labelling ratio) is included in the legend. The precision of all of the sixteen datasets is tightly clustered around the precision expected when varying SNR alone.

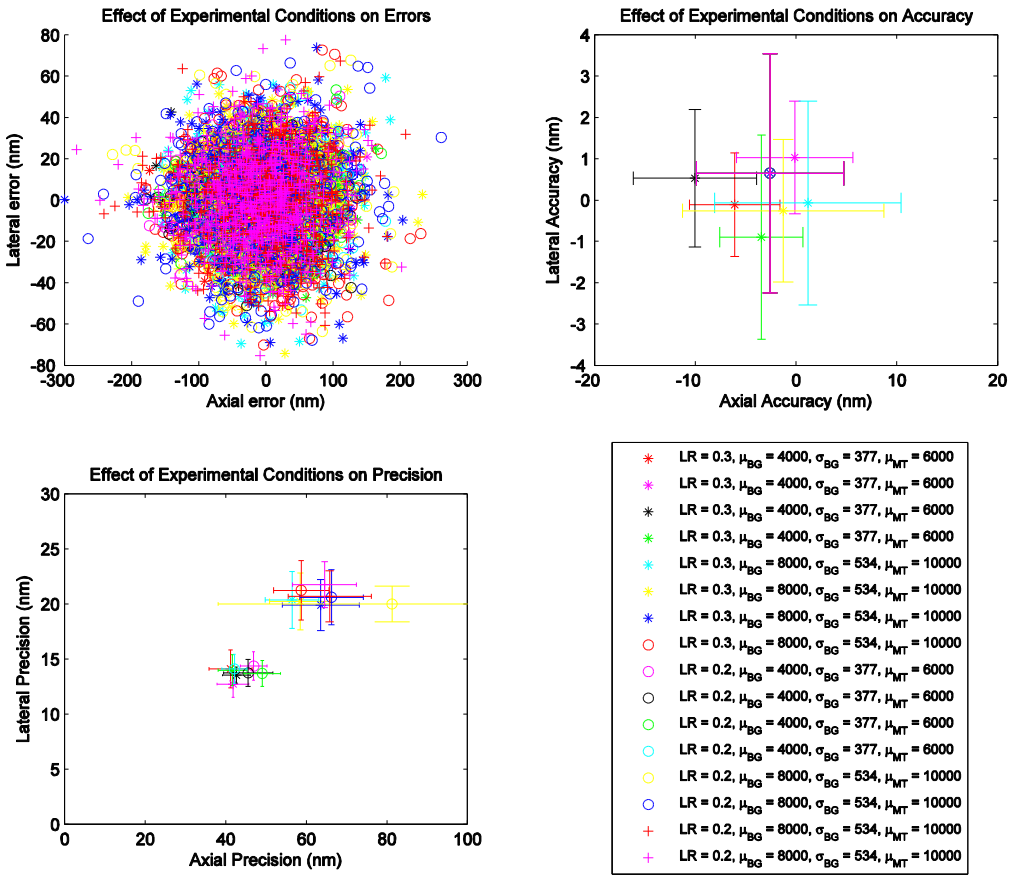

Figure 17: The prediction of the tracking accuracy and precision at experimentally relevant parameter values. *The axial and lateral errors are plotted along with the accuracy and precision for different experimentally relevant parameter values. The two most significant values are shown in the legend, the others can be found in the Appendix. The precision is again strongly correlated with the SNR resulting in two distinct clusters. Error bars are standard Errors*

3.3 Mean Square Displacement Analysis

3.3.1 MSD of Simulated Tracks

Having the ability to characterise the error associated with tracking allows some constraints to be put on the MSD curve. The following analysis was performed on 100, 200s long microtubule growth episodes using the Monte Carlo method, sampled at a time interval of 0.5s. The mean velocity was 50nm s^{-1}, the diffusion coefficient was 700nm^2s^{-1} and a localisation error with σ=50 nm was put on the tracks after sampling. **Figure 18** shows the output of the modified MSD program including evidence of directed motion in the form of a velocity autocorrelation and power spectral density. A parabolic fit (Equation 9) weighted by the inverse of the standard deviation was made to the mean MSD curve. The resulting measure for the diffusion coefficient with 95% confidence intervals was 735 [732-738] nm^2s^{-1}. The theory suggests that for this amount of data the real diffusion coefficient should be reliably estimated however after many trials this is not the case. Looking at the predictions for the velocity and the error (49.9 [49.9 49.9]nm s^{-1} and 70 [71 73] respectively) it becomes apparent that the fit could be constrained by knowledge of the error prior to making the fit. In this case the error was simulated, and so known, and does indeed constrain the fit to give the correct value for the diffusion coefficient.

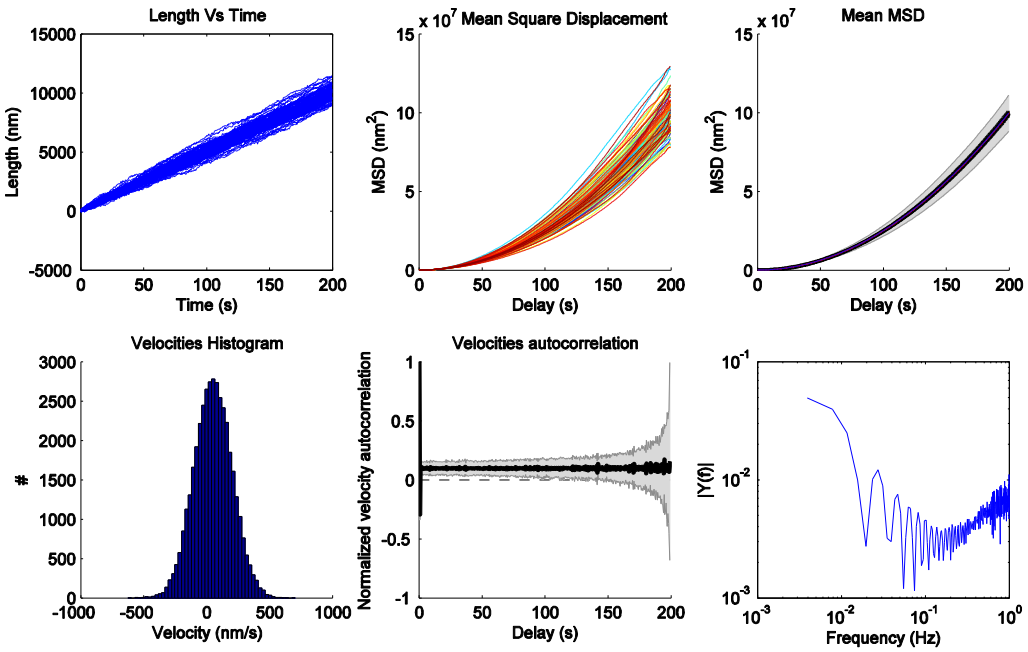

Figure 18: MSD analysis of simulated MT growth. *(Top Left) length vs Time for 100 Mt tracks 200 seconds long sampled at 0.5s intervals. (Top Middle) All MSD curves (Top Right) Mean MSD curve, with standard deviation in grey and error bars for SE as defined in Section 2.2.3. (Bottom Left) Velocities histogram (Middle Bottom) Velocities autocorrelation, which has non zero value due to directed growth (Bottom Right) Power Spectral Density calculated from the velocities autocorrelation showing deviation from pure Brownian motion.*

3.3.2 Derivation of exposure time correction

If we wish to constrain the MSD curve with an estimate of the error it is important to consider the effect that exposure time has on the MSD offset. It is known from single particle tracking studies that the MSD is modified by a constant offset when averaging positions over an exposure time[23,69–71] however no one has published a derivation of this effect in the presence of drift, or in this case directed growth. This derivation is based on that given by Michalet, (2010)[23] for pure Brownian motion.

Consider dividing the frame of duration Δt into m steps of length δt. The effect of the exposure time can be derived using the average length of a fraction λ of the steps in the frame such that $t_E = \lambda m \delta t$. Then the average length in during exposure and therefore the measured length is given by

$$\bar{L}_q = L_0 + \sum_{j=1}^{q-1} \frac{q-j}{q} \Delta L_j, \tag{23}$$

where $\{\Delta L_j\}$ are the steps taken at each δt and $q = \lambda m$.

$$\langle \Delta L_j \rangle = v \delta t, \tag{24}$$

$$\langle \Delta L_i \Delta L_j \rangle = (2D\delta t + v^2 \delta t^2)\delta_{ij}, \tag{25}$$

where δ_{ij} is the Kronecker Delta which can be used since individual steps are i.i.d.

The displacement for any frames separated by k can be calculated from the measured lengths in each frame including the sum of all ΔL_j between the frames of interest,

$$\bar{L}_q^{(k+1)} - \bar{L}_q^{(1)} = \sum_{i=1}^{k} \sum_{j=1}^{m} \Delta L_j^{(i)} + \sum_{j=1}^{q-1} \frac{q-j}{q} \Delta L_j^{(k+1)} - \sum_{j=1}^{q-1} \frac{q-j}{q} \Delta L_j^{(1)}, \tag{26}$$

$$= \sum_{i=2}^{k} \sum_{j=1}^{m} \Delta L_j^{(i)} + \sum_{j=1}^{q-1} \frac{q-j}{q} \Delta L_j^{(k+1)} + \sum_{j=1}^{q-1} \frac{j}{q} \Delta L_j^{(1)} + \sum_{j=q}^{m} \Delta L_j^{(1)}, \tag{27}$$

The average square of this expression is taken and the cross terms cancel due to the Kronecker Delta so,

$$\langle \left(\bar{L}_q^{(k+1)} - \bar{L}_q^{(1)} \right)^2 \rangle = \left(\sum_{i=2}^{k} \sum_{j=1}^{m} 1 + \sum_{j=1}^{q-1} \left(\frac{q-j}{q} \right)^2 - \sum_{j=1}^{q-1} \left(\frac{j}{q} \right)^2 + \sum_{j=q}^{m} 1 \right) \langle \Delta L^2 \rangle, \tag{28}$$

since $\langle \Delta L^2 \rangle = (2D\delta t + v^2 \delta t^2)$, we can do some algebra, take the limit as m goes to infinity and arrive at the expression for mean square displacement,

$$\langle \Delta L^2 \rangle = t^2 v^2 + 2Dt - \frac{2}{3} D t_E - \frac{1}{3} t_E^2 v^2 \quad (29)$$

To which localisation noise can be added as previously shown.

4 Discussion and Conclusions

Microtubule dynamics are unlikely to be governed by the simplistic mechanisms and expressions presented in this report and even much more detailed models struggle to reproduce behaviours observed in experiment. In order to fully understand microtubule kinetics there is a need for very high quality data to inform these models and allow them to progress. Often this comes at the cost of simple validation of the methods used check the results of experiments. In this report I have presented a simulation that is designed to test one such method. The assumptions made about the end definition in the simulation may need revision, as suggested by the taper length and exposure time biases, however it has proven useful in analysing MDA. It also demonstrates a marked improvement on the previous model convolution method in being able to simulate the effect of camera exposure time and the ease of manipulation of the MT on the nanoscale prior to rendering. It is also an improvement both in terms of computational efficiency and truer to life representation of fluorescence. The Monte Carlo simulation of length should now be integrated into the simulation so that the exposure time can be directly simulated rather than approximated.

MDA has been shown to be very accurate in the context of a *dynamic* MT tip tracker rather than previous methods for tracking stabilised MTs. Simulations have shown that SNR is a dominating aspect of tip tracking using MDA and there are many trade-offs which will allow improvements in signal to noise at the detriment to some other experimental quality. For example the exposure time could be increased to decrease the SNR but this results in possibly significantly large bias in the measurement of the MT end.

Another interesting question arises with regard to the labelling ratio is what criterion or boundary has been crossed when the labelling ratio drops below 15% that results in the rapid decrease in accuracy while the precision behaves entirely linearly.

It seems very probable that accurate estimates for the errors in MT tip tracking for specific experiments could be calculated using the methods in this report. This would allow the constraining of an MSD curve providing more accurate estimates of the diffusion coefficient.

5 Acknowledgements

I would like to acknowledge first my supervisors Dr Thomas Surrey and Dr Lewis Griffin for there help and for giving up there time to offer this project. A really big thank you to Grego Bohner who wrote the MDA tracking program providing the motivation for this project.

6 References

1. Alberts, B., Johnson, A. & Lewis, J. *Molecular Biology of the Cell.* (Garland Science, 2002). at <http://www.ncbi.nlm.nih.gov/books/NBK26907/>

2. Lodish, H. *et al. Molecular Cell Biology*. (W. H. Freeman, 2000). at <http://www.ncbi.nlm.nih.gov/books/NBK21475/>

3. Wade, R. H. On and around microtubules: an overview. *Mol. Biotechnol.* **43,** 177–191 (2009).

4. Mitchison, T. J. Localization of an exchangeable GTP binding site at the plus end of microtubules. *Science* **261,** 1044–7 (1993).

5. Mitchison, T. J. & Kirschner, M. Dynamic instability of microtubule growth. *Nature* **312,** 237–242 (1984).

6. Howard, J. & Hyman, A. A. Growth, fluctuation and switching at microtubule plus ends. *Nat. Rev. Mol. Cell Biol.* **10,** 569–574 (2009).

7. Gardner, M. K., Zanic, M. & Howard, J. Microtubule catastrophe and rescue. *Curr. Opin. Cell Biol.* **25,** 14–22 (2013).

8. Conde, C. & Cáceres, A. Microtubule assembly, organization and dynamics in axons and dendrites. *Nat. Rev. Neurosci.* **10,** 319–32 (2009).

9. Seligmann, J. & Twelves, C. Tubulin: an example of targeted chemotherapy. *Future Med. Chem.* **5,** 339–52 (2013).

10. Desai, A. & Mitchison, T. J. Microtubule Polymerization Dynamics. *Annu. Rev. Cell Dev. Biol.* **13,** 83–117 (1997).

11. Carter, S. L., Eklund, A. C., Kohane, I. S., Harris, L. N. & Szallasi, Z. A signature of chromosomal instability inferred from gene expression profiles predicts clinical outcome in multiple human cancers. *Nat. Genet.* **38,** 1043–8 (2006).

12. Ravelli, R. B. G. *et al.* Insight into tubulin regulation from a complex with colchicine and a stathmin-like domain. *Nature* **428,** 198–202 (2004).

13. Pecqueur, L. *et al.* A designed ankyrin repeat protein selected to bind to tubulin caps the microtubule plus end. *Proc. Natl. Acad. Sci. U. S. A.* **109,** 12011–6 (2012).

14. Maurer, S. P., Fourniol, F. J., Bohner, G., Moores, C. A. & Surrey, T. EBs recognize a nucleotide-dependent structural cap at growing microtubule ends. *Cell* **149,** 371–82 (2012).

15. Abbe, E. Beiträge zur Theorie des Mikroskops und der mikroskopischen Wahrnehmung. *Arch. für mikroskopische Anat.* **9,** 413–418 (1873).

16. Bieling, P., Telley, I. a, Hentrich, C., Piehler, J. & Surrey, T. *Fluorescence microscopy assays on chemically functionalized surfaces for quantitative imaging of microtubule, motor, and +TIP dynamics. Methods Cell Biol.* **95,** 555–80 (Elsevier, 2010).

17. Bates, M., Huang, B. & Zhuang, X. Super-resolution microscopy by nanoscale localization of photo-switchable fluorescent probes. *Curr. Opin. Chem. Biol.* **12,** 505–14 (2008).

18. Henriques, R. & Mhlanga, M. M. PALM and STORM: What hides beyond the Rayleigh limit? *Biotechnol. J.* **4,** 846–857 (2009).

19. Gardner, M. K. *et al.* Rapid microtubule self-assembly kinetics. *Cell* **146,** 582–92 (2011).

20. Demchouk, A. O., Gardner, M. K. & Odde, D. J. Microtubule Tip Tracking and Tip Structures at the Nanometer Scale Using Digital Fluorescence Microscopy. *Cell. Mol. Bioeng.* **4,** 192–204 (2011).

21. Ruhnow, F., Zwicker, D. & Diez, S. Tracking single particles and elongated filaments with nanometer precision. *Biophys. J.* **100,** 2820–8 (2011).

22. Maurer, S. P. *et al.* EB1 Accelerates Two Conformational Transitions Important for Microtubule Maturation and Dynamics. *Curr. Biol.* **24,** 372–384 (2014).

23. Michalet, X. Mean square displacement analysis of single-particle trajectories with localization error: Brownian motion in an isotropic medium. *Phys. Rev. E* **82,** 041914 (2010).

24. Qian, H., Sheetz, M. P. & Elson, E. L. Single particle tracking. Analysis of diffusion and flow in two-dimensional systems. *Biophys. J.* **60,** 910–21 (1991).

25. Berglund, A. J. Statistics of camera-based single-particle tracking. *Phys. Rev. E* **82,** 011917 (2010).

26. Gould, T. J., Hess, S. T. & Bewersdorf, J. Optical nanoscopy: from acquisition to analysis. *Annu. Rev. Biomed. Eng.* **14,** 231–54 (2012).

27. Bohner, G., Gustafsson, N. & Surrey, T. Tracking Dynamic Microtubule Ends With Close-to-Nanometre Precision. *Prep.* (2014).

28. Einstein, A. Investigations on the theory of the brownian movement. *Ann. Phys.* **322,** 549–560 (1905).

29. Castle, B. T. & Odde, D. J. Brownian dynamics of subunit addition-loss kinetics and thermodynamics in linear polymer self-assembly. *Biophys. J.* **105,** 2528–40 (2013).

30. Gittes, F., Mickey, B., Nettleton, J. & Howard, J. Flexural rigidity of microtubules and actin filaments measured from thermal fluctuations in shape. *J. Cell Biol.* **120,** 923–34 (1993).

31. Wells, D. B. & Aksimentiev, A. Mechanical properties of a complete microtubule revealed through molecular dynamics simulation. *Biophys. J.* **99,** 629–37 (2010).

32. Brangwynne, C. P., MacKintosh, F. C. & Weitz, D. a. Force fluctuations and polymerization dynamics of intracellular microtubules. *Proc. Natl. Acad. Sci. U. S. A.* **104,** 16128–33 (2007).

33. Feynman, R. P., Leighton, R. B. & Sands, M. *The Feynman Lectures on Physics. Vol. II*. (Addison-Wesley, 1964).

34. Nawrotek, A., Knossow, M. & Gigant, B. The determinants that govern microtubule assembly from the atomic structure of GTP-tubulin. *J. Mol. Biol.* **412,** 35–42 (2011).

35. Zovko, S., Abrahams, J. P., Koster, A. J., Galjart, N. & Mommaas, A. M. Microtubule Plus-End Conformations and Dynamics in the Periphery of Interphase Mouse Fibroblasts. *Mol. Biol. Cell* **19,** 3138–3146 (2008).

36. Schek, H. T., Gardner, M. K., Cheng, J., Odde, D. J. & Hunt, A. J. Microtubule assembly dynamics at the nanoscale. *Curr. Biol.* **17,** 1445–55 (2007).

37. Valiron, O., Arnal, I., Caudron, N. & Job, D. GDP-tubulin incorporation into growing microtubules modulates polymer stability. *J. Biol. Chem.* **285,** 17507–13 (2010).

38. Fourniol, F. J. *et al.* Template-free 13-protofilament microtubule-MAP assembly visualized at 8 A resolution. *J. Cell Biol.* **191,** 463–70 (2010).

39. Caplow, M. & Shanks, J. Evidence that a single monolayer tubulin-GTP cap is both necessary and sufficient to stabilize microtubules. *Mol. Biol. Cell* **7,** 663–75 (1996).

40. Hill, T. L. Introductory analysis of the GTP-cap phase-change kinetics at the end of a microtubule. *Proc. Natl. Acad. Sci. U. S. A.* **81,** 6728–32 (1984).

41. Coombes, C. E., Yamamoto, A., Kenzie, M. R., Odde, D. J. & Gardner, M. K. Evolving tip structures can explain age-dependent microtubule catastrophe. *Curr. Biol.* **23,** 1342–8 (2013).

42. Odde, D. J., Cassimeris, L. & Buettner, H. M. Kinetics of microtubule catastrophe assessed by probabilistic analysis. *Biophys. J.* **69,** 796–802 (1995).

43. Bowne-Anderson, H., Zanic, M., Kauer, M. & Howard, J. Microtubule dynamic instability: a new model with coupled GTP hydrolysis and multistep catastrophe. *Bioessays* **35,** 452–61 (2013).

44. O'Brien, E. T. *et al.* Dynamic Instability of Individual Microtubules Analyzed by Video Light Microscopy: Rate Constants and Transition Frequencies. *J. Cell Biol.* **107,** 1437–1448 (1988).

45. Duellberg, C. Mechanism and Control of Microtubule Dynamic Instability Probed by in Vitro Reconstitutions and Microfluidics Approaches. (2014).

46. Fygenson, D. K. Microtubules: The Rhythm of Assembly and the Evolution of Form. (1995).

47. Vitre, B. *et al.* EB1 regulates microtubule dynamics and tubulin sheet closure in vitro. *Nat. Cell Biol.* **10,** 415–21 (2008).

48. Akhmanova, A. & Steinmetz, M. O. Microtubule +TIPs at a glance. *J. Cell Sci.* **123,** 3415–9 (2010).

49. Castoldi, M. & Popov, A. V. Purification of brain tubulin through two cycles of polymerization-depolymerization in a high-molarity buffer. *Protein Expr. Purif.* **32,** 83–8 (2003).

50. Hyman, a *et al.* Preparation of modified tubulins. *Methods Enzymol.* **196,** 478–85 (1991).

51. Jaqaman, K. *et al.* Robust single-particle tracking in live-cell time-lapse sequences. *Nat. Methods* **5,** 695–702 (2008).

52. Bieling, P. *et al.* Reconstitution of a microtubule plus-end tracking system in vitro. *Nature* **450,** 1100–5 (2007).

53. Prahl, L. S., Castle, B. T., Gardner, M. K. & Odde, D. J. *Quantitative analysis of microtubule self-assembly kinetics and tip structure. Methods Enzymol.* **540,** 35–52 (Elsevier Inc., 2014).

54. Oosawa, F. Size distribution of protein polymers. *J. Theor. Biol.* **27,** 69–86 (1970).

55. Skellam, J. G. The frequency distribution of the difference between two Poisson variates belonging to different populations. *J.R. Stat. Soc.* **109,** 296 (1946).

56. Wang, H. Y., Elston, T., Mogilner, a & Oster, G. Force generation in RNA polymerase. *Biophys. J.* **74,** 1186–202 (1998).

57. Hill, T. L. Effect of fluctuating surface structure and free energy on the growth of linear tubular aggregates. *Biophys. J.* **49,** 1017–31 (1986).

58. Chrétien, D., Fuller, S. D. & Karsenti, E. Structure of growing microtubule ends: two-dimensional sheets close into tubes at variable rates. *J. Cell Biol.* **129,** 1311–28 (1995).

59. VanBuren, V., Cassimeris, L. & Odde, D. J. Mechanochemical model of microtubule structure and self-assembly kinetics. *Biophys. J.* **89,** 2911–26 (2005).

60. VanBuren, V., Odde, D. J. & Cassimeris, L. Estimates of lateral and longitudinal bond energies within the microtubule lattice. *Proc. Natl. Acad. Sci. U. S. A.* **99,** 6035–40 (2002).

61. Breiman, L. Bagging predictors. *Mach. Learn.* **24,** 123–140 (1996).

62. Metropolis, N. & Ulam, S. The Monte Carlo Method. *J. Am. Stat. Assoc.* **44,** (1949).

63. Fall, C. P., Marland, E. S., Wagner, J. M. & Tyson, J. J. *Computational Cell Biology*. (Springer, 2005).

64. Pitman, J. *Probability*. (Springer, 1993).

65. Press, W. H., Teukolsky, S. A., Vetterling, W. T. & Flannery, B. *Numerical Recipies in C*. (Cambridge Univeristy Press, 2007).

66. Saxton, M. J. Modeling 2D and 3D diffusion. *Methods Mol. Biol.* **400,** 295–321 (2007).

67. Tarantino, N. *et al.* TNF and IL-1 exhibit distinct ubiquitin requirements for inducing NEMO-IKK supramolecular structures. *J. Cell Biol.* **204,** 231–45 (2014).

68. Hirsch, M., Wareham, R. J., Martin-Fernandez, M. L., Hobson, M. P. & Rolfe, D. J. A stochastic model for electron multiplication charge-coupled devices--from theory to practice. *PLoS One* **8,** e53671 (2013).

69. Montiel, D., Cang, H. & Yang, H. Quantitative characterization of changes in dynamical behavior for single-particle tracking studies. *J. Phys. Chem. B* **110,** 19763–70 (2006).

70. Savin, T. & Doyle, P. Role of a finite exposure time on measuring an elastic modulus using microrheology. *Phys. Rev. E* **71,** 041106 (2005).

71. Goulian, M. & Simon, S. M. Tracking single proteins within cells. *Biophys. J.* **79,** 2188–98 (2000).

72. Matsumoto, M. & Nishimura, T. Mersenne twister: a 623-dimensionally equidistributed uniform pseudo-random number generator. *ACM Trans. Model. Comput. Simul.* **8,** 3–30 (1998).

7 Appendix

A. Taper Lengths in the 1D model

The average behaviour of the taper length with respect to time was simulated using the method in Appendix 7B with the modification that each event that occurred was randomly assigned, with uniform probability, to have occurred on one of 13 protofilaments. This was done under two different parameter sets, the mean of the range of published values outlined in Appendix 7C, and the 10 fold higher values proposed by Gardner et. al. 2011[19]. The taper length was defined as $TL = \max\left(L_{\mathrm{pf}}(t)\right) - \min(L_{\mathrm{pf}}(t))$ and a mean of $N = 1000$ tracks was calculated. This mean is empirically identical to $\langle \sigma_L \rangle \cdot \sqrt{11}$ where σ_L is the standard deviation of the protofilament lengths. This factor is a correction for the bias in the mean arising from the use of 2 out of 13 values to estimate of the standard deviation. Equivalently $TL^2 \cdot 11$ is equal to the variance. 2D model simulations (Fig A) have however had more success predicting the taper length seen in experiment (Fig B,C)[41].

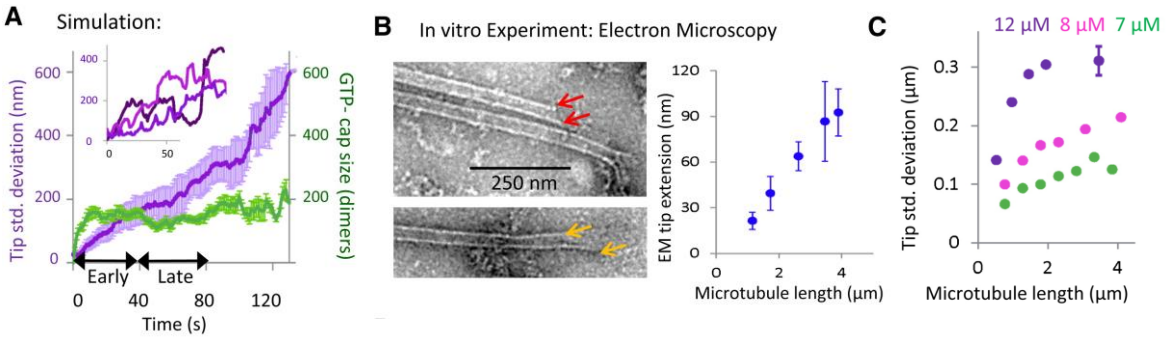

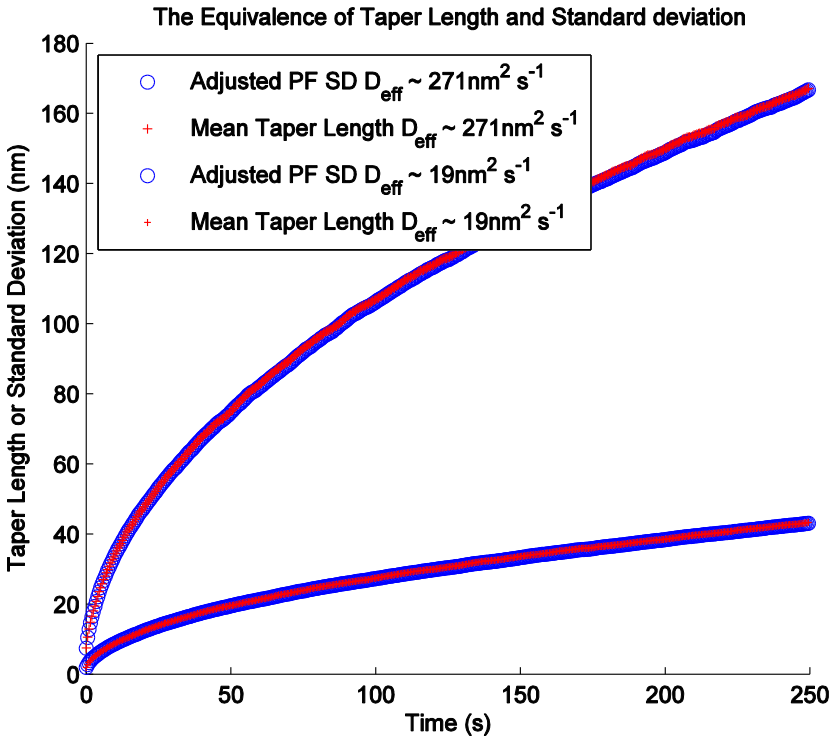

B. Monte Carlo Simulation of Length

Monte Carlo methods[62] are a class of computational algorithms useful for stochastic simulations of systems which can be described as a Markov Chain. The generalised pattern of implementation begins with a deterministic computation being performed on repeated random samples from a probability density function, followed by aggregation of the results. Large numbers of repeated random samples were performed using the Mersenne twister random number generator (MATLAB) proposed by Matsumoto and Nishimura (1998)[72].

The following summarises the specific formulism implemented for the continuous time 1D model, based on the probability density function of the dwell times between events[63].

Let $p_n(t)$ be the probability at time t that there are exactly $N(t) = n$ subunits in the MT. At a micro-time step δt later, $t' = t + \delta t$ the probability of $N(t') = n$ is given by $p_n(t + \delta t) = p_n + \Delta$ where Δ is some small correction. We assume that δt is small such that only one event has occurred and that only one subunit can be lost or added per event. From the properties of a continuous time Markov chain there are three mutually exclusive events possible which are independent of n and proportional to δt. So we can say

$$\begin{aligned} p_n(t+\delta t) = \text{Prob}[n(t) = n;\ \text{and no event has occurred}] \\ + \text{Prob}[n(t) = n-1; \text{and a subunit has been added}] \\ + \text{Prob}[n(t) = n+1; \text{and a subunit has been lost}]. \end{aligned} \quad 30$$

It follows from the assumption of proportionality to time that $k_+\delta t$ and $k_-\delta t$ are the probabilities of subunit addition and loss respectively in time δt allowing us to write,

$$\begin{aligned} p_n(t+\delta t) &= p_n(t)(1-(k_+ + k_-)\delta t) + p_{n-1}(t)k_+\delta t + p_{n+1}(t)k_-\delta t \\ &= p_n(t) + \delta t[k_+ p_{n-1}(t) + k_- p_{n+1}(t) - (k_+ + k_-)p_n(t)] \end{aligned} \quad 31$$

where $(1-(k_+ + k_-)\delta t)$ is the probability that no event has occurred.

Taking the limit $\delta t \to 0$

$$\lim_{\delta t \to 0} \frac{p_n(t+\delta t) - p_n(t)}{\delta t} = \frac{dp_n(t)}{dt} = -(k_+ + k_-)p_n(t) + k_+ p_{n-1}(t) + k_- p_{n+1}(t) \quad 32$$

and it is clear that Equation 31 is nothing else but the forward Eular method for solving the differential equation which governs the evolution of $p_n(t)$ providing an algorithm for calculating the probabilities at all later times given $p_n(t)$ is known, for all n, at time t.

To demonstrate this, consider an MT with exactly m subunits at time t. This defines $p_m(t) = 1$ and $p_{n\neq m}(t) = 0$. The dwell time at this position will be a random variable $\mathcal{T}$ for which we can define a probability density $\mathcal{F}_{\mathcal{T}}(\tau)$ with support $\tau \in [0, \infty)$. To do this consider the probability $q(\tau)$, that no event has occurred in $t \in [t, t+\tau]$, from equation 32,

$$\begin{aligned} \frac{dq(\tau)}{dt} &= -(k_+ + k_-)q(\tau) \\ &\Rightarrow q(\tau) = \exp[-(k_+ + k_-)\tau]. \end{aligned} \quad 33$$

The probability of at least one event in $t \in [t, t+\tau]$ defines $\mathcal{F}_{\mathcal{T}}(\tau)$ as follows,

$$\begin{aligned} 1 - q(\tau) &= \text{Prob}[\mathcal{T} < \tau] = \int_0^\tau \mathcal{F}_{\mathcal{T}}(\tau')d\tau' \\ \Rightarrow \mathcal{F}_{\mathcal{T}}(\tau) &= (k_+ + k_-)\exp[-(k_+ + k_-)\tau] \end{aligned} \quad 34$$

Which is exponentially distributed with mean $1/(k_+ + k_-)$ as expected for the distribution of times between Poisson distributed events.

Random values are sampled from this distribution of dwell times[65] provides a sequence of times $\{t_i\} = t_{i-1} + \mathcal{T}_i;\ i = 1,2,\dots,k$, at which events (addition or loss of a subunit) have occurred. The type of event at each time is determined by a logical test on a uniformly distributed random variable $R \in [0,1]$ with the following criterion,

$$N(t_i) = \begin{cases} N(t_{i-1}) + 1 \leftrightarrow R_i < k_+/(k_+ + k_-) \\ N(t_{i-1}) - 1 \leftrightarrow R_i > k_+/(k_+ + k_-) \end{cases} \quad 35$$

C. Published association/dissociation rates

On Rate k_+ $(\mu M^{-1}\, s^{-1})$	Off Rate k_+ $(\mu M^{-1}\, s^{-1})$	REF:
3.9±1.8	25.7±7.1	Engelborghs et al. 1977
7.2	17	Bergen and Borisy 1980
1.00±0.36	2.00±0.18	Farrell and Jordan 1982
4.2	2.3	Carlier et al. 1984
3.82	0.37	Mitchison and Kirschner 1984
1.4		Gard and Kirschner 1987
8.9±0.3	44±14	Walker et al. 1988
6.8	25-30	O'Brien et al. 1990
3	0.1	Drechsel et al. 1992
6.9±0.5	32±6.0	Trinczek et al. 1993
5	0.1	Hyman et al. 1992*
5.7	14.1	Chretien et al. 1995
4.9±2.3	0.49±0.12	Brouhard et al. 2008*
5.1	3.9	Gardner et al. 2011*
4.8	**13.0**	**Mean**

*measured for GMPCPP-tubulin

D. Parameters used for TIRF data simulations

All of the following parameter sets were used to produce N=750 frames (15 movies of 50 frames) for tracking.

Experiment	BackGround Mean	BackGround std	Signal Mean	Labelling Ratio	std of Lateral Deflection	Exposure Time	Taper Length	Pixel Size	kon	koff	[Tub]	Vg	Dp
Experimental Conditions	4000	377	6000	0.300	150	200	192	120	4.80	13.00	14.23	34.01	15.38
	4000	377	6000	0.300	150	200	192	120	60.50	708.00	12.00	11.07	271.19
	4000	377	6000	0.300	150	300	192	120	60.50	708.00	12.00	11.07	271.19
	4000	377	6000	0.300	150	300	192	120	4.80	13.00	14.23	34.01	15.38
	8000	534	10000	0.300	150	200	192	120	60.50	708.00	12.00	11.07	271.19
	8000	534	10000	0.300	150	200	192	120	4.80	13.00	14.23	34.01	15.38
	8000	534	10000	0.300	150	300	192	120	60.50	708.00	12.00	11.07	271.19
	8000	534	10000	0.300	150	300	192	120	4.80	13.00	14.23	34.01	15.38
	4000	377	6000	0.200	150	200	192	120	60.50	708.00	12.00	11.07	271.19
	4000	377	6000	0.200	150	200	192	120	4.80	13.00	14.23	34.01	15.38
	4000	377	6000	0.200	150	300	192	120	60.50	708.00	12.00	11.07	271.19
	4000	377	6000	0.200	150	300	192	120	4.80	13.00	14.23	34.01	15.38
	8000	534	10000	0.200	150	200	192	120	60.50	708.00	12.00	11.07	271.19
	8000	534	10000	0.200	150	200	192	120	4.80	13.00	14.23	34.01	15.38
	8000	534	10000	0.200	150	300	192	120	60.50	708.00	12.00	11.07	271.19
	8000	534	10000	0.200	150	300	192	120	4.80	13.00	14.23	34.01	15.38
Exposure Time, True End	0	0	2000	1.000	0	0	0	120	N.A.	N.A.	N.A.	50.00	0.00
	0	0	2000	1.000	0	150	0	120	N.A.	N.A.	N.A.	50.00	0.00
	0	0	2000	1.000	0	300	0	120	N.A.	N.A.	N.A.	50.00	0.00
	0	0	2000	1.000	0	450	0	120	N.A.	N.A.	N.A.	50.00	0.00
Exposure Time, Visible End	7000	0	9000	1.000	0	150	0	120	N.A.	N.A.	N.A.	50.00	0.00
	7000	0	9000	1.000	0	450	0	120	N.A.	N.A.	N.A.	50.00	0.00
	7000	0	9000	1.000	0	300	0	120	N.A.	N.A.	N.A.	50.00	0.00

Growth Fluctuation with Labelling Ratio	0	0	2000	0.100	0	0	0	120	N.A.	N.A.	N.A.	50.00	0.00
	0	0	2000	0.100	0	0	0	120	N.A.	N.A.	N.A.	50.00	1000.00
	7000	0	9000	0.100	0	0	0	120	N.A.	N.A.	N.A.	50.00	400.00
	7000	0	9000	0.100	0	0	0	120	N.A.	N.A.	N.A.	50.00	800.00
	0	0	2000	0.100	0	0	0	120	N.A.	N.A.	N.A.	80.00	3000.00
Growth Fluctuation	7000	0	9000	1.000	0	0	0	120	N.A.	N.A.	N.A.	50.00	0.00
	7000	0	9000	1.000	0	0	0	120	N.A.	N.A.	N.A.	50.00	20.00
	7000	0	9000	1.000	0	0	0	120	N.A.	N.A.	N.A.	50.00	40.00
	7000	0	9000	1.000	0	0	0	120	N.A.	N.A.	N.A.	50.00	80.00
	7000	0	9000	1.000	0	0	0	120	N.A.	N.A.	N.A.	50.00	1000.00
	7000	0	9000	1.000	0	0	0	120	N.A.	N.A.	N.A.	50.00	500.00
Growth Speed	7000	0	9000	1.000	0	0	0	120	N.A.	N.A.	N.A.	0.00	0.00
	7000	0	9000	1.000	0	0	0	120	N.A.	N.A.	N.A.	25.00	0.00
	7000	0	9000	1.000	0	0	0	120	N.A.	N.A.	N.A.	50.00	0.00
	7000	0	9000	1.000	0	0	0	120	N.A.	N.A.	N.A.	100.00	0.00
Growth Speed with Labelling Ratio	0	0	2000	0.100	0	0	0	120	N.A.	N.A.	N.A.	0.00	0.00
	0	0	2000	0.100	0	0	0	120	N.A.	N.A.	N.A.	25.00	0.00
	0	0	2000	0.100	0	0	0	120	N.A.	N.A.	N.A.	50.00	0.00
	0	0	2000	0.100	0	0	0	120	N.A.	N.A.	N.A.	75.00	0.00
Labelling Ratio	0	0	2000	0.025	0	0	0	120	N.A.	N.A.	N.A.	50.00	0.00
	7000	0	9000	0.050	0	0	0	120	N.A.	N.A.	N.A.	50.00	0.00
	0	0	2000	0.100	0	0	0	120	N.A.	N.A.	N.A.	50.00	0.00
	7000	0	9000	0.150	0	0	0	120	N.A.	N.A.	N.A.	50.00	0.00
	0	0	2000	0.175	0	0	0	120	N.A.	N.A.	N.A.	50.00	0.00
	7000	0	9000	1.000	0	0	0	120	N.A.	N.A.	N.A.	50.00	0.00
	0	0	2000	0.250	0	0	0	120	N.A.	N.A.	N.A.	50.00	0.00
	7000	0	9000	0.300	0	0	0	120	N.A.	N.A.	N.A.	50.00	0.00
	0	0	2000	0.500	0	0	0	120	N.A.	N.A.	N.A.	50.00	0.00
	0	0	2000	1.000	0	0	0	120	N.A.	N.A.	N.A.	50.00	0.00

Labelling Ratio With Noise	2000	267	4000	0.150	0	0	0	120	N.A.	N.A.	N.A.	50.00	0.00
	2000	267	4000	0.250	0	0	0	120	N.A.	N.A.	N.A.	50.00	0.00
	2000	267	4000	0.350	0	0	0	120	N.A.	N.A.	N.A.	50.00	0.00
	5000	422	7000	0.150	0	0	0	120	N.A.	N.A.	N.A.	50.00	0.00
	5000	422	7000	0.250	0	0	0	120	N.A.	N.A.	N.A.	50.00	0.00
	8000	534	10000	0.150	0	0	0	120	N.A.	N.A.	N.A.	50.00	0.00
	8000	534	10000	0.250	0	0	0	120	N.A.	N.A.	N.A.	50.00	0.00
	8000	534	10000	0.350	0	0	0	120	N.A.	N.A.	N.A.	50.00	0.00
	5000	422	7000	0.350	0	0	0	120	N.A.	N.A.	N.A.	50.00	0.00
Lateral Deflection	7000	0	9000	1.000	0	0	0	120	N.A.	N.A.	N.A.	50.00	0.00
	7000	0	9000	1.000	50	0	0	120	N.A.	N.A.	N.A.	50.00	0.00
	7000	0	9000	1.000	150	0	0	120	N.A.	N.A.	N.A.	50.00	0.00
	7000	0	9000	1.000	300	0	0	120	N.A.	N.A.	N.A.	50.00	0.00
Best Case	7000	0	9000	1.000	0	0	0	120	N.A.	N.A.	N.A.	0.00	0.00
Orientation	7000	0	9000	1.000	0	0	0	120	N.A.	N.A.	N.A.	50.00	0.00
Pixel Size	7000	0	9000	1.000	0	0	0	75	N.A.	N.A.	N.A.	50.00	0.00
	7000	0	9000	1.000	0	0	0	100	N.A.	N.A.	N.A.	50.00	0.00
	7000	0	9000	1.000	0	0	0	120	N.A.	N.A.	N.A.	0.00	0.00
	7000	0	9000	1.000	0	0	0	140	N.A.	N.A.	N.A.	50.00	0.00
Position	7000	0	9000	1.000	0	0	0	120	N.A.	N.A.	N.A.	50.00	0.00
	7000	0	9000	1.000	0	0	0	120	N.A.	N.A.	N.A.	50.00	0.00
SNR	0	0	2000	1.000	0	0	0	120	N.A.	N.A.	N.A.	50.00	0.00
	2000	276	4000	1.000	0	0	0	120	N.A.	N.A.	N.A.	50.00	0.00
	5000	422	7000	1.000	0	0	0	120	N.A.	N.A.	N.A.	50.00	0.00
	6000	462	8000	1.000	0	0	0	120	N.A.	N.A.	N.A.	50.00	0.00
	7000	500	9000	1.000	0	0	0	120	N.A.	N.A.	N.A.	50.00	0.00
	8000	534	10000	1.000	0	0	0	120	N.A.	N.A.	N.A.	50.00	0.00
	12000	655	14000	1.000	0	0	0	120	N.A.	N.A.	N.A.	50.00	0.00
Taper Length	7000	0	9000	1.000	0	0	0	120	N.A.	N.A.	N.A.	0.00	0.00

	7000	0	9000	1.000	0	0	96	120	N.A.	N.A.	N.A.	50.00	0.00
	0	0	2000	1.000	0	0	192	120	N.A.	N.A.	N.A.	50.00	0.00
	7000	0	9000	1.000	0	0	288	120	N.A.	N.A.	N.A.	50.00	0.00
	7000	0	9000	1.000	0	0	480	120	N.A.	N.A.	N.A.	50.00	0.00
	7000	0	9000	1.000	0	0	672	120	N.A.	N.A.	N.A.	50.00	0.00
Taper Length With Noise	7000	500	9000	1.000	0	0	0	120	N.A.	N.A.	N.A.	50.00	0.00
	7000	500	9000	1.000	0	0	96	120	N.A.	N.A.	N.A.	50.00	0.00
	7000	500	9000	1.000	0	0	192	120	N.A.	N.A.	N.A.	50.00	0.00
	7000	500	9000	1.000	0	0	288	120	N.A.	N.A.	N.A.	50.00	0.00